International Journal of Thermofluids 28 (2025) 101315

Contents lists available at ScienceDirect

International Journal of Thermofluids

journal homepage: www.sciencedirect.com/journal/international-journal-of-thermofluids

Magnetohydrodynamics phenomena in continuous casting process under applied electromagnetic braking (EMBr)

Alexander Vakhrushev [a], Ebrahim Karimi-Sibaki [b], Menghuai Wu [b], Mohamad Al Nasser [a], Gernot Hackl [c], Yong Tang [c], Josef Watzinger [d], Jan Boháček [e], Abdellah Kharicha [a,b,*]

[a] Christian Doppler Laboratory for Metallurgical Applications of Magnetohydrodynamics, University of Leoben, Franz-Josef Strasse 18, Leoben 8700, Austria
[b] Chair of Simulation and Modeling of Metallurgical Processes, University of Leoben, Franz-Josef Strasse 18, Leoben 8700, Austria
[c] RHI Magnesita Technology Center, Magnesitstrasse 2, Leoben A-8700, Austria
[d] Primetals Technologies Austria GmbH, Turmstrasse 44, Linz A-4031, Austria
[e] Heat Transfer and Fluid Flow Laboratory, Brno University of Technology, Brno 61669, Czech Republic

ARTICLE INFO

Keywords:
Continuous casting (CC)
Electromagnetic braking (EMBR)
Magnetohydrodynamics (MHD)
Free-surface
Solidification
Turbulence

ABSTRACT

In the presented work the effects of electromagnetic braking (EMBr) are gathered, exemplifying key magnetohydrodynamics (MHD) phenomena in continuous casting (CC) process. The complex interactions between turbulent liquid metal flows and a direct current (DC) magnetic field through the meso-to-macro scale cascade are reviewed. We analyze MHD influences on different types of melt motion in CC, including jets, recirculation zones, and shear flows, as well as Lorentz force-induced acceleration in stagnant regions. These phenomena result from the distribution of induced electric current lines closing through either the liquid bulk or the semiconducting solidifying shell. The continuously growing shell, formed against the water-cooled copper mold walls, is significantly affected by the hot melt flow patterns. The study highlights practical applications of EMBr to optimize flow dynamics in the CC process, providing insight into improving casting stability and product quality.

1. Introduction

The continuous casting (CC) process integrates several critical stages, beginning with the persistent feeding of molten steel through a refractory submerged entry nozzle (SEN) into the mold, followed by the solidification and growth of the solid shell along the cooled mold walls, and concluding with the controlled extraction of a semi-solid slab [1–3]. The inherently complex nature of this process has been described metaphorically by Lee at al., [1] as a "butterfly effect," emphasizing how small variations in initial casting conditions can lead to significant impacts on the final slab quality. Numerical modeling approaches, span from detailed high-fidelity computational fluid dynamics (CFD) simulations capturing turbulence, heat transfer, solidification, and inclusion dynamics [4] to computationally efficient reduced-order models that simplify complex physical phenomena into manageable frameworks [5], have become crucial tools for analyzing and optimizing CC operations.

A detailed numerical study by Wu et al. [6] analyzed the flow-solidification interaction in CC, highlighting the significant roles of superheat-induced remelting, advection of latent heat in the mushy zone, and enhanced turbulence-induced energy dissipation in influencing the formation of the solidified shell. Computational modeling of fluid flow in CC molds by Thomas [7] and a detailed investigations by Yang et al. [8] as well as by Cho et al. [9] using multiphase CFD, supported by plant measurements and laboratory-scale experiments, have elucidated critical defect formation mechanisms. These studies demonstrate that poor control of fluid flow parameters, particularly at the meniscus, significantly increases the risks of shell thinning, surface defects, meniscus hooks, slag entrainment and particle entrapment in solidified steel. A comprehensive numerical model by Ramirez-Lopez at al., [10,11] explicitly simulating transient slag infiltration, shell solidification, and mold oscillation demonstrated a direct correlation between slag layer dynamics and oscillation-induced shell thickness variations, revealing mechanisms responsible for critical casting defects such as oscillation marks and transverse cracks.

Torres-Alonso et al. [12,13] conducted a two-part experimental and numerical investigation into oscillating jet flows and their influence on meniscus stability in thin slab casting (TSC) molds using a full-scale water model and advanced Reynolds stress model (RSM) coupled with

* Corresponding author.
E-mail address: abdellah.kharicha@unileoben.ac.at (A. Kharicha).

https://doi.org/10.1016/j.ijft.2025.101315

Available online 22 June 2025

the volume of fluid (VOF) method. Their studies revealed that self-sustained oscillations of the liquid steel jets, discharging from a standard two-port SEN were a persistent phenomenon across different casting speeds, mold widths, and SEN immersion depths. A very recent work of Xiao et al. [14] combined large eddy simulation (LES) with the VOF method to investigate transient slag entrainment due to steel jet oscillation in slab CC for a straight bottom-open SEN. The study revealed a strong correlation between casting speed, mold width and jet oscillation, enhancing slag entrainment. In contrast, SEN submergence depth had a limited influence on oscillation frequency and entrainment rate.

Electromagnetic braking (EMBr) is a widely employed method of controlling the liquid melt flow in the CC mold. This process involves the utilization of direct current (DC) magnetic fields, which may have either uniform or locally varying distributions [15,16]. The purpose of this process is to mitigate turbulence intensity and stabilize transient flow structures. Such EMBr control techniques are essential in modern CC practices to achieve high-quality steel products. A systematic CFD study by Hosseini and Amani [17] demonstrated that the optimized combination of a single-ruler EMBr positioned below the SEN and local EMBr near meniscus effectively reduces surface velocities and fluctuations, significantly improves superheat transport and uniformity of solidified shell growth, and prevents detrimental flow patterns in TSC.

Vakhrushev et al. [18] applied a fully coupled model integrating LES turbulence modeling, solidification, and magnetohydrodynamic (MHD) effects to analyze asymmetric melt flow in TSC process. Their simulations demonstrated that while EMBr stabilized turbulent jets, it could enlarge asymmetries, shifting shell remelting zones deeper into the slab. The study highlighted the necessity of adjustable EMBr configurations to manage transient flow asymmetry effectively. Furthermore, Wang et al. [19] extended the MHD studies of TSC mold flow under varying single-ruler EMBr intensities to reveal that, as magnetic induction intensity increased, the flow pattern evolved from a classic double-roll to a transitional three-roll and eventually to a single-roll or plug-like structure.

Lu et al. [20] combined solidification, MHD, and Lagrangian particle tracking. In their study, the flow field exhibited strong asymmetry and instability in the absence of EMBr, leading to pronounced shell thickness variation and elevated inclusion entrapment. The application of a double-ruler EMBr in the meniscus and jet regions significantly improved flow symmetry and reduced turbulent fluctuations. Further increasing the upper magnetic flux density stabilized the flow, enhancing shell uniformity and lowering the inclusion capture rate. However, excessive braking suppressed meniscus velocity below optimal levels, potentially hindering superheat delivery. To extend previous studies, Cui et al. [21] conducted a comprehensive investigation into MHD effects in an ultra-high-speed thin slab casting process, evaluating three EMBr configurations: the conventional ruler type, an improved local design, and a newly proposed bowl-type EMBr. Among these, the bowl-type EMBr demonstrated superior control by evenly suppressing turbulent jet penetration, stabilizing the meniscus, and improving both the thickness and uniformity of the solidified shell. Overall, the authors provided critical insights into the interplay between EMBr design, casting parameters, and metallurgical outcomes in high-speed TSC.

A recent numerical investigation by Wang et al. [22], employing a Eulerian–Lagrangian approach, demonstrated that the combined application of EMBr and electromagnetic stirring (EMS) effectively suppresses the entrapment of argon bubbles and non-metallic inclusions in slab CC, highlighting the critical role of Archimedes electromagnetic forces in accurately predicting inclusion behavior. Najafian Ashrafi et al. [23] experimentally studied mold flow under traveling magnetic fields using a 1-to-6 scale mini-LIMMCAST model and ultrasound Doppler velocimetry (UDV). They found that different EMS modes induced distinct flow phenomena, including jet deflection, intensified surface velocities, reverse flows, jet narrowing, and asymmetric or three-dimensional structures. It was shown that the observed patterns are not simple superpositions of EMS and jet flows. The magnetic force number has been asserted as a key dimensionless parameter for predicting mold flow behavior.

In previous studies, the focus has been placed on specific phenomena or effects. In the present work we novelly combine the fundamental MHD phenomena and their cascading effects across micro- to macroscales into a unified discussion to elucidate the influence of EMBr during the CC process along with the aspects of the modelling techniques. As analytically studied by Davidson [24], the application of a DC magnetic field to conductive fluids leads to strong coupling between the induced electric current density and the turbulent flow. While small-scale vortices are suppressed and their momentum redistributed into the mean flow, isotropic turbulence reorganizes into large quasi-2D coherent vortices aligned with magnetic field lines, as shown by Kobayashi [25]. The Lorentz force does act against fluid motion, as originally intended in the EMBr technique; however, it also accelerates the fluid in quiescent regions. This dual effect leads to momentum redistribution and flattening of jet-like flows along the magnetic field direction, accompanied by adjacent reverse flow zones, as detailed in the works of Kharicha and Vakhrushev et al. [26,27]. The closure of induced currents, either within the liquid bulk or through the semiconducting solid in flows confined by the CC mold, is identified as the mechanism behind these effects [28]. Consequently, the turbulent motion of a conductive melt, as well as the corresponding free-surface flows at the top of the mold, becomes either unstable or strongly damped under MHD forces, as analyzed by Cho and Thomas [29]. Under certain conditions, they may also exhibit transient behavior, with secondary flow structures forming near the die meniscus, reported in Vakhrushev et al. [30].

Hereon, we highlight how the applied EMBr magnetic field suppresses small-scale turbulence, reorganizes mesoscale flow structures such as jets and recirculation zones, and ultimately reshapes large-scale flow patterns and solidification behavior across the MHD cascade. In the following sections, we present the details of the numerical model and provide prominent application cases that investigate complex EMBr-driven effects in continuous casting.

2. Numerical model

In this section, we present the numerical model developed to capture the magnetohydrodynamic effects induced by the applied DC magnetic field in the turbulent flow of liquid steel, including the associated free surface dynamics and solidification phenomena within the continuous casting mold.

The following notations are utilized in the present work: bold symbols are used to indicate vector and tensor variables (e.g., velocity $\boldsymbol{u}$, viscous stress $\boldsymbol{\tau}_{\mathrm{lam}}$); the italic notations correspond to scalar variables (e.g., pressure p, density ρ); and symbols in the normal font are used to indicate the constants (e.g., characteristic length L_0, magnetic permeability μ_0).

To begin, the governing equations for the unsteady turbulent flow of a conductive fluid under an applied magnetic field, according to the mass and momentum conservation, are given as follows:

$$\frac{\partial \rho}{\partial t} + \nabla \bullet \rho \boldsymbol{u} = 0, \tag{1}$$

$$\rho\left[\frac{\partial \boldsymbol{u}}{\partial t} + \nabla \bullet (\boldsymbol{u} \otimes \boldsymbol{u})\right] = -\nabla p + \rho \boldsymbol{g} + \nabla \bullet \boldsymbol{\tau}_{\mathrm{lam}} - \nabla \bullet \boldsymbol{\tau}_{\mathrm{SGS}} + \boldsymbol{F}_{\mathrm{L}} + \boldsymbol{F}_{\mathrm{surf}}, \tag{2}$$

where ρ is the density of the liquid, $\boldsymbol{u}$ is the velocity vector, p is the pressure, $\boldsymbol{g}$ is the gravitational acceleration. The terms $\boldsymbol{\tau}_{\mathrm{lam}}$ and $\boldsymbol{\tau}_{\mathrm{SGS}}$ correspond to the laminar and subgrid-scale (SGS) Reynolds stresses, respectively. The external Lorentz ($\boldsymbol{F}_{\mathrm{L}}$) and surface tension ($\boldsymbol{F}_{\mathrm{surf}}$) forces, acting on a fluid, will be discussed and numerically disclosed in corresponding sections.

It must be noted that we give more flavor to the MHD modeling description, as it serves as a cornerstone of our present investigations. In contrast, the remaining components of the coupled numerical model, such as solidification and free surface tracking, are described more concisely, as they follow standard approaches established in our previous work or in literature. Nevertheless, selected features are discussed in greater detail where relevant.

2.1. Modeling MHD turbulence

Modeling turbulence in CC processes is crucial for accurately predicting fluid flow, heat transfer, and associated phenomena like inclusion transport, meniscus instability, and solidification behavior. Two widely applied numerical techniques for capturing turbulent flow in industrial-scale simulations are the Reynolds-averaged Navier-Stokes (RANS) and large eddy simulation (LES) approaches.

The RANS method models turbulence by averaging flow quantities and using closure models, such as the standard k–ε [31] and realizable k–ε [32], or the shear-stress transport (SST) k–ω models [33], making it computationally efficient for engineering use. However, it smooths out transient turbulent structures, limiting accuracy in complex flows. In contrast, LES resolves large-scale eddies directly and models only the smaller scales [34,35], offering improved accuracy for capturing unsteady, anisotropic, and unstable flows typical in CC, though at a significantly higher computational cost.

A series of detailed experimental and numerical investigations have significantly advanced the understanding of transient flow behavior and electromagnetic flow control in CC molds. Chaudhary [36] et al. conducted a comprehensive comparison of six turbulence modeling approaches, including steady and unsteady RANS (URANS) as well as LES models, against UDV data obtained from a GaInSn liquid-metal model of a CC. Their results showed that LES methods provided the most accurate predictions of both mean flow and transient features, including jet wobbling and high-frequency velocity fluctuations. Through proper orthogonal decomposition (POD) analysis, the study revealed that alternating swirl in the nozzle bottom was a key mechanism responsible for the observed transient jet behavior. Kratzsch et al. [37] performed comprehensive numerical investigations of CC mold flow using URANS simulations. Their results showed that advanced turbulence models (particularly RNG k–ε [38] and k–ω SST), combined with higher-order discretization schemes, accurately captured critical flow characteristics such as asymmetric jet spreading and long-term coherent oscillations. In contrast, simulations using the standard and realizable k–ε models exhibited unstable behavior and significant deviations from the experiment. A recent detailed study by Vakhrushev et al. [39], based on the 1-to-2 under-scaled water model measurements, demonstrated the effectiveness of advanced URANS modeling in capturing complex turbulent flow phenomena, including flow oscillations and separations in a single-port SEN for TSC, highlighting the critical influence of mesh quality and boundary-layer treatment on URANS simulation accuracy.

Building on the reviewed findings in non-MHD turbulence modeling, Miao et al. [40] investigated the behavior of turbulent melt flow under EMBr influence using a modified RANS-SST turbulence model, validated by UDV measurements. They highlighted that velocity fluctuations misaligned with the magnetic field are damped, leading to directional turbulence suppression and continuous decay of turbulent kinetic energy. This drives a reorganization of the flow into elongated, anisotropic eddies aligned with the field. To capture these effects, turbulence models must account for the dimensionality shift introduced by Joule dissipation, as strong magnetic fields induce a quasi-two-dimensional flow structure in place of typical three-dimensional isotropic turbulence. When applied to the URANS approach, the necessity of introducing an additional anisotropy variable (α_μ), as proposed by Widlund et al. [41], was elucidated, along with the important role of mold wall electrical conductivity. Thomas et al. [42] significantly advanced the topic by exploring the effect of single-ruler EMBr positioning on CC mold flow dynamics using LES simulations and experimental validation. In a subsequent study, Kratzsch et al. [43] employed a hybrid LES / RANS turbulence model, specifically the SAS approach, to analyze MHD flow in a CC mold under EMBr. The SAS method captured transient jet behavior and flow oscillations more accurately than URANS; however, it required higher mesh resolution near the SEN and jet regions. The study highlighted SAS as an effective compromise between accuracy and computational cost for modeling MHD-affected turbulent flows in casting.

Together, these studies underline the value of advanced turbulence modeling, particularly LES, and the complex interaction between the DC magnetic fields, flow instabilities, and boundary conditions in modeled continuous casting processes. As initially highlighted by Kabayashi [25] and validated in subsequent studies, reviewed in this section, LES provides a more reliable representation of turbulent structures and their interaction with magnetic fields, making it an essential approach for MHD modeling. Generally, the SGS turbulent stress tensor $\boldsymbol{\tau}_{SGS}$ is estimated as:

$$\boldsymbol{\tau}_{SGS} = -2{\cdot}C_{SGS}{\cdot}(\Delta_{SGS})^2{\cdot}|\boldsymbol{D}|{\cdot}\boldsymbol{D}, \tag{3}$$

defined by the rate-of-strain tensor $\boldsymbol{D} = \frac{1}{2}\left(\nabla\boldsymbol{u} + \nabla^{\mathrm{T}}\boldsymbol{u}\right)$ and its norm $|\boldsymbol{D}| = \sqrt{2\boldsymbol{D}:\boldsymbol{D}}$, with C_{SGS} as the model parameter and Δ_{SGS} as the filter width in the LES simulation.

The wall-adapting local eddy-viscosity (WALE) model, commonly used in LES, provides enhanced accuracy for complex geometries and maintains robustness under mesh refinement [44]. By accounting for both strain effects and small-scale rotation, it naturally adapts to Lorentz force influences in MHD modeling. Moreover, the WALE subgrid-scale (SGS) model effectively captures the formation of coherent turbulent structures aligned with magnetic field lines [25]. For these reasons, it is employed by the present authors for turbulent MHD flow modeling in the current study.

2.2. Conservative MHD formulation

MHD flows are characterized by a set of dimensionless numbers. One of the key parameters is the magnetic Reynolds number ($\mathscr{R}m$), which describes the relative importance of magnetic field advection by the conductive flow in comparison to magnetic diffusion. It indicates whether induced currents significantly alter the magnetic field distribution within the fluid and is calculated as:

$$\mathscr{R}m = \frac{\text{Induction}}{\text{Diffusion}} = \mathrm{u}_0{\cdot}\mathrm{L}_0{\cdot}\mu_0{\cdot}\sigma_0 \tag{4}$$

for the characteristic velocity u_0, domain half-thickness L_0 with the fluid electrical conductivity σ_0 and the magnetic permeability $\mu_0 = 4\pi \cdot 10^{-7}\mathrm{H/m}$.

At low magnetic Reynolds numbers ($\mathscr{R}m \ll 1$), which are typical for the magnetic field intensities used in the CC process, the electric potential method [24] is applied. This numerical approach is used in MHD modeling to compute the induced electric current density ($\boldsymbol{j}$) in conductive flows under the influence of an applied magnetic field ($\boldsymbol{B}_0$). Due to the negligible magnetic induction effects at low $\mathscr{R}m$, the total magnetic field ($\boldsymbol{B}$) is assumed to be equal to the applied field ($\boldsymbol{B}_0$). By introducing the electric scalar potential (φ), Ohm's law can be written in the following form:

$$\boldsymbol{j} = \sigma{\cdot}(-\nabla\varphi + \boldsymbol{u}\times\boldsymbol{B}_0), \tag{5}$$

where σ stands for electrical conductivity. Substituting Ohm's law from Eq. (5) into the charge conservation equation $\nabla{\bullet}\boldsymbol{j} = 0$ yields a Poisson equation for the electric potential:

$$\nabla \bullet (\sigma\,\nabla\varphi) = \nabla \bullet (\sigma{\cdot}(\boldsymbol{u}\times\boldsymbol{B}_0)). \tag{6}$$

The Lorentz force ($\boldsymbol{F}_L$) acting on the conductive fluid under the applied magnetic field is estimated as:

$$\boldsymbol{F}_{\mathrm{L}} = \boldsymbol{j} \times \boldsymbol{B}_0. \tag{7}$$

The system of Navier-Stoks Eq. (1)-(2) coupled with the electric potential model (5)-(6) is discretized using the finite volume method (FVM) and solved with an in-house code implemented in the open-source CFD software OpenFOAM® [45].

For discretization, Rhie-Chow interpolation [46] is employed to avoid pressure-velocity decoupling [47] on collocated unstructured meshes used in OpenFOAM®. This approach is also used in the present study to construct a conservative form of the MHD equations. Ni et al. [48] proposed a scheme for decomposing the non-conservative body force into global and local conservative terms. According to this method, the integral form of the Lorentz force given in Eq. (7) can be expanded as:

$$\int_{\Omega} \boldsymbol{j} \times \boldsymbol{B}_0 \, \mathrm{d}\omega = -\oint_{\Gamma} \boldsymbol{n} \bullet (\boldsymbol{j} \otimes (\boldsymbol{B}_0 \times \boldsymbol{r})) \, \mathrm{d}s \; - \; \boldsymbol{r} \times \oint_{\Gamma} \boldsymbol{n} \bullet (\boldsymbol{j} \otimes \boldsymbol{B}_0) \, \mathrm{d}s, \tag{8}$$

where $\boldsymbol{r}$ denotes the coordinate vector of an integration point P in the Eulerian frame of reference, and $\boldsymbol{\Omega}$ is a volume bounded by the surface Γ with outward normal vector $\boldsymbol{n}$. The geometric details illustrating the transition from volume to surface integrals are provided schematically in Fig. 1(a).

The discrete form of the surface integrals on the right-hand side (RHS) of Eq. (8) is derived in this section for an arbitrary polyhedral cell, shown in Fig. 1(b), with volume Ω_C and corresponding face areas A_f. The center of mass of the control volume (CV) is denoted by C, while f refers to the face centers. The coordinate vectors of the cell and face centers are denoted as $\boldsymbol{r}_C$ and $\boldsymbol{r}_f$, respectively.

Accurate discretization is crucial for capturing MHD boundary layers while preserving physical conservation laws. Accordingly, we proceed by transforming the cell-centered formulation $(\boldsymbol{j} \times \boldsymbol{B}_0)|_C$ for the Lorentz force using the RHS surface integral form of Eq. (8). Following the FVM approach by Ni et al. [48], detailed in Mas de les Valls Ortiz's PhD thesis [49], the normal current density flux (j_{n}) is computed from the normal gradient of the electric potential ($\nabla_{\mathrm{n}}\varphi$) across each CV face area (A_f):

$$j_{\mathrm{n}} = -\sigma_f \cdot (\nabla_{\mathrm{n}}\varphi) \cdot A_f + \chi, \tag{9}$$

and the induced magnetic flux (χ), which is estimated at the CV face centers as

$$\chi = \boldsymbol{n} \bullet \left(\sigma_f \cdot (\boldsymbol{u}_f \times \boldsymbol{B}_{0f})\right) \cdot A_f, \tag{10}$$

based on the values of electrical conductivity (σ_f), melt velocity ($\boldsymbol{u}_f$), and the applied magnetic field ($\boldsymbol{B}_{0,f}$) interpolated from the control volume centroid C the face center f (see schematics in Fig. 1(b)).

Finally, a conservative form of the Lorentz force is assembled at the finite volume center C by discretizing a surface integral in Eq. (8) over the control volume Ω_C as a sum for all face centers f:

$$\boldsymbol{F}_{\mathrm{L}}|_C = -\frac{1}{\Omega_C} \left(\sum_f j_{\mathrm{n}} \cdot (\boldsymbol{B}_{0f} \times \boldsymbol{r}_f) + \boldsymbol{r}_C \times \left(\sum_f j_{\mathrm{n}} \cdot \boldsymbol{B}_{0f} \right) \right), \tag{11}$$

where $\boldsymbol{r}_f$ and $\boldsymbol{r}_C$ are face and cell center coordinates, illustrated in Fig. 1 (b).

As demonstrated in Vakhrushev et al. [28], the conductance ratio of the solidified shell significantly influences the distribution of the induced electric current, causing the current loops to close through the more conductive solid region and thereby affecting the braking strength. Therefore, accurate interpolation of the electrical conductivity at the liquid melt / solid shell boundary is essential. To ensure that the interpolated value (σ_f) reflects the better-conducting solid material, we apply:

$$\sigma_f|_{\mathrm{liq/solid}} = \max\{\sigma_{C,\ \mathrm{own}},\ \sigma_{C,\ \mathrm{neigh}}\}, \tag{12}$$

where the maximum conductivity is selected between the cell-centered values of the face's owner cell ($\sigma_{C,\mathrm{own}}$) and its neighboring cell ($\sigma_{C,\mathrm{neigh}}$), following the in OpenFOAM® notation (see Fig. 1(b)).

2.3. Free surface tracking

The volume of fluid (VOF) approach is used to track the free surface [50]. This approach is integrated with a novel magnetohydrodynamic model that accounts for the varying electrical conductivity in the multiphase regions, such as liquid, solid and gas, as reflected in Eq. (5)-(6) [30]. The free surface evolution is determined by an advection equation for the scalar marker function (α):

$$\frac{\partial \alpha}{\partial t} + \nabla \bullet (\boldsymbol{u} \cdot \alpha) = 0. \tag{13}$$

The continuum surface force (CSF) technique [51] is used to incorporate surface tension forces into the momentum Eq. (2), represented as:

$$\boldsymbol{F}_{\mathrm{surf}} = \gamma \cdot \kappa \cdot \boldsymbol{n}, \tag{14}$$

where γ is the surface tension, $\boldsymbol{n}$ is the interface normal vector, and κ is the curvature of the interface. It is worth mentioning that all physical properties used are linearly interpolated between different phases based on α-function. A detailed numerical implementation and the coupling of MHD and VOF methods is given in Vakhrushev et al. [30].

It should be noted that standard linear interpolation in the VOF method leads to an overestimation of electrical conductivity, as explicitly demonstrated in Fig. 2 by Vakhrushev et al. [30]. Due to the extremely high electrical conductivity of Galinstan [52], at least 15 orders of magnitude greater than air, even small liquid fractions dominate the conductivity calculation. As a result, in MHD simulations with surface tracking, the induced electric current does not properly detect non-conductive interfaces, such as entrapped gas bubbles or slag droplets. To resolve this issue, harmonic interpolation is applied between the electrical conductivities of the melt (σ_{melt}) and the secondary,

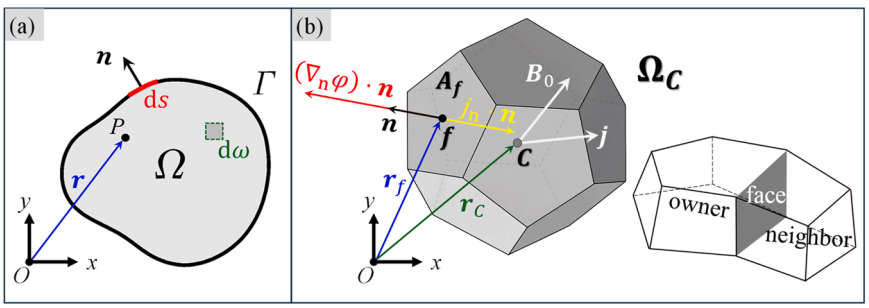

Fig. 1. Schematics of (a) a physical control volume Ω bounded by surface Γ and (c) an arbitrary polyhedral computational cell used in the FVM discretization with owner / neighbor notation.

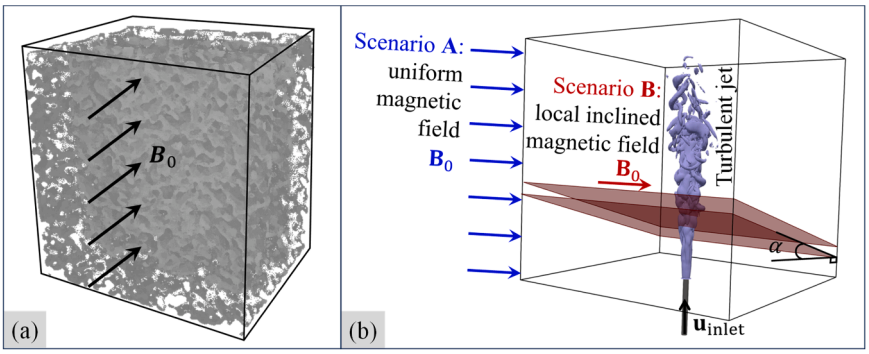

Fig. 2. Setups to analyze the MHD effects on turbulence: (a) an isotropic turbulence under a uniform magnetic field; (b) submerged turbulent jet exposed to a uniform magnetic field (Scenario A) and to a localized inclined magnetic field (Scenario B).

low-conductivity phase, such as air (σ_{air}):

$$\sigma(\alpha) = 1/[\alpha / \sigma_{melt} + (1-\alpha) / \sigma_{air}], \tag{15}$$

which closely approximates a step function. This ensures that the induced electric current density remains confined to the conductive melt pool and is effectively blocked at non-conductive interfaces.

2.4. Simulating solidification

To incorporate solidification effects, the energy equation is formulated in its general advection-diffusion form, accounting for total enthalpy (H):

$$\rho\left[\frac{\partial H}{\partial t} + \nabla \bullet (\boldsymbol{u} \cdot H)\right] = \nabla \bullet \left(\lambda_{eff} \cdot \nabla T\right), \tag{16}$$

where λ_{eff} represents effective thermal conductivity, incorporating turbulent effects. The total enthalpy H is calculated as:

$$H = \int C_p \, dT + (1 - f_s) \cdot \mathscr{L}. \tag{17}$$

where C_p is the specific heat, f_s is the solid fraction, and $\mathscr{L}$ is the latent heat of fusion.

The modified momentum Eq. (2), accounting for the presence of the solidifying shell under an applied magnetic field, is expressed as:

$$\rho\left[\frac{\partial \boldsymbol{u}}{\partial t} + \nabla \bullet (\boldsymbol{u} \otimes \boldsymbol{u})\right] = \nabla \bullet \boldsymbol{\tau}^{tot} - \nabla p + \rho \boldsymbol{g} + \boldsymbol{F}_L + \boldsymbol{F}_{surf}. \tag{18}$$

where the total deviatoric stress tensor ($\boldsymbol{\tau}^{tot}$) is a blend of the solid ($\boldsymbol{\tau}^{sol}$) and liquid contributions, weighted by their respective phase fractions f_s and f_ℓ:

$$\boldsymbol{\tau}^{tot} = f_s \cdot \boldsymbol{\tau}^{sol} + f_\ell \cdot (\boldsymbol{\tau}_{lam} - \boldsymbol{\tau}_{SGS}), \tag{19}$$

with the condition $f_s + f_\ell \equiv 1$.

As described by Rappaz, Bellet, and Deville [53], metallic alloys exhibit fully viscoplastic behavior above two-thirds of their melting temperature, a condition relevant to the CC mold region and the subsequent slab part. The viscoelasticity of the alloy, which represents rate-dependent unrecovered deformations, is described by the Ostwald-de-Waele or Norton–Hoff law [54]:

$$\boldsymbol{\tau}^{sol} = 2K\left(\sqrt{3}\ \dot{\varepsilon}_{eq}\right)^{m-1} \boldsymbol{D}, \tag{20}$$

where the viscoplastic consistency K and strain rate sensitivity m are experimentally obtained model parameters; $\boldsymbol{D}$ is the strain rate tensor, previously defined as the symmetric part of $\nabla \boldsymbol{u}$; the equivalent strain rate is defined as $\dot{\varepsilon}_{eq} = \sqrt{2/3\boldsymbol{D} : \boldsymbol{D}}$.

This approach was applied by Vakhrushev et al. [55], where a viscoplastic deformation model was implemented to simulate the withdrawal of the solidified shell in a funnel-type continuous casting mold, and was subsequently coupled with magnetohydrodynamic effects induced by EMBr in a follow-up study [56].

3. Modelling results

The presented numerical model was employed to investigate the interaction between MHD forces and various types of turbulent flow occurring during the continuous casting process with an applied electromagnetic brake. In our results section, we begin by addressing fundamental phenomena at the scale of turbulent coherent structures, as well as recirculation zones and conductive melt jets, and then progressively advance to global flow phenomena occurring in the continuous casting mold.

3.1. Interaction of DC magnetic field with turbulence and conductive jets

To analyze the MHD effects in continuous casting, it is essential to first examine the fundamental interactions between a DC magnetic field and anisotropic turbulence, as well as its influence on the dominant flow structures. One of the most critical features in CC mold flows is the submerged turbulent jet, which forms as fresh melt is fed through the SEN ports. Such jets typically form a classical double-roll recirculation pattern when confined within the mold cavity. Understanding how magnetic fields alter this behavior is key to interpreting and controlling MHD-influenced flow dynamics in the CC process.

The setups used to investigate these two fundamental MHD interactions are illustrated in Fig. 2. Fig. 2(a) shows a turbulence box subjected to a uniform DC magnetic field, serving as a simplified configuration to observe the suppression and anisotropic reorganization of turbulent eddies under the Lorentz force. Fig. 2(b) presents a submerged turbulent jet in two scenarios: Scenario **A** applies a uniform magnetic field orthogonal to the jet axis, while Scenario **B** introduces a localized, inclined DC magnetic field. These configurations enable us to isolate and analyze the effects of magnetic field distribution and orientation on jet behavior, turbulence damping, and flow restructuring.

Initially, the application of a unidirectional magnetic field dampens small-scale eddies in fully developed turbulent flows, illustrated in Fig. 3 (a). These small eddies, particularly those with velocity components perpendicular to the magnetic field, are subjected to Joule (Ohmic) dissipation, which acts to suppress their intensity. As this suppression occurs, the momentum formerly carried by these small-scale structures is redistributed into the larger-scale mean flow. This energy redistribution leads to a reorganization of the turbulence field, transforming initially isotropic turbulence into quasi-2D coherent structures aligned with the magnetic field lines, as shown in Fig. 3(b). This restructuring plays a critical role in modifying transport processes, including mixing and heat transfer.

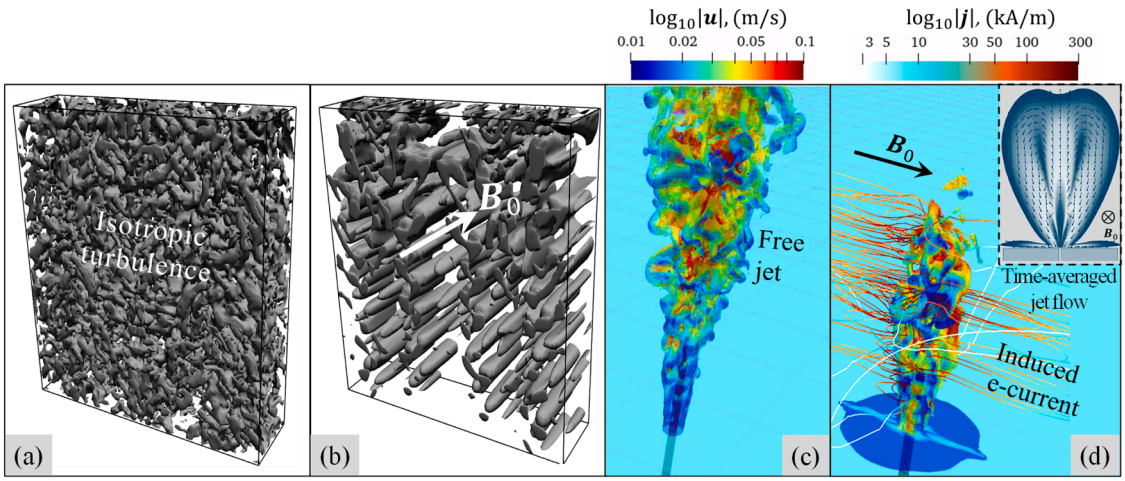

Fig. 3. Turbulent MHD effects: (a) isotropic turbulence; (b) quasi-2D coherent structures under an applied magnetic field. Submerged turbulent jet flow: (c) without and (d) with the applied DC magnetic field. The top right corner shows the time-averaged MHD jet with reverse flow zones [26].

At a larger scale (see Fig. 3(c)–(d)), the structure of the turbulent jet flow is governed by the collective action of the Lorentz force under the applied uniform DC magnetic field, corresponding to the Scenario **A** in Fig. 2(b). The MHD force inherently opposes fluid motion. As a result, the breakup length of the submerged turbulent jet observed in Fig. 3(c) is significantly reduced under the braking effect of the applied magnetic field, as shown in Fig. 3(d). This phenomenon was investigated numerically by Kharicha et al. [26], building on the theoretical framework proposed by Davidson [57]. Interestingly, the fluid in quiescent regions is also accelerated due to the closure of induced electric current loops. This leads to a redistribution of momentum and a flattening of jet-like streams along the direction of the magnetic field lines, as clearly illustrated in Fig. 3(d). Furthermore, this process is accompanied by the formation of adjacent reverse flow zones, resulting from the entrainment of bulk liquid to compensate for the increased jet cross-section and maintain throughput. The time-averaged velocity vector field, shown in the upper-right corner of Fig. 3(d), illustrates these effects and highlights the complex flow restructuring induced by MHD interactions [24,26].

However, in industrial applications like EMBr in the CC process, idealized conditions, such as uniform magnetic fields oriented perfectly orthogonal to the flow axis or planes, are rarely encountered. In practice, the applied magnetic field $\boldsymbol{B}_0$ often exhibits a localized distribution with an inclination angle α that deviates from 90° Scenario **B**, schematically illustrated in Fig. 2(b), is specifically designed to investigate such cases.

Vakhrushev et al. [58] developed a novel 3D large eddy simulation model to analyze the interaction of a turbulent conductive jet with a localized, transverse magnetic field, bridging industrial applications and astrophysical jet physics. The study systematically investigated how magnetic field strength, jet inclination angle, and jet confinement influence jet refraction, reflection, and turbulence modulation based on the interaction (Stuart) number, which defines the ratio between electromagnetic and inertial forces:

$$\mathcal{N} = \frac{\sigma \cdot L_0 \cdot |\boldsymbol{B}_0|^2}{\rho \cdot U_0}, \tag{21}$$

where σ is the electrical conductivity, L_0 and U_0stand for the characteristic domain length and flow velocity, and ρ denotes fluid's density.

As shown by the dimensionless analysis results in Fig. 4 for Scenario **B** (illustrated in Fig. 2(b)), increasing the interaction number $\mathcal{N}$ leads to a progressive transformation of the conductive jet behavior. As $\mathcal{N}$ grows, the jet experiences refraction (Fig. 4(b)-(d)) due to the influence of the inclined magnetic field, resulting in increasingly complex flow dynamics. These include the emergence of reverse flow zones [26], the formation of secondary jets flowing in the opposite direction, and a noticeable bending of the main stream under the action of the Lorentz force. With further intensification of the MHD interaction, the flow ultimately undergoes a full reflection (Fig. 4(e)), indicating a complete redirection of the jet away from its initial path. This transition highlights the strong influence of localized and inclined magnetic fields on jet stability and symmetry.

3.2. MHD effects in CC mold flow with applied EMBr

In this section, we investigate how the fundamental MHD phenomena discussed above manifest in the context of the continuous casting

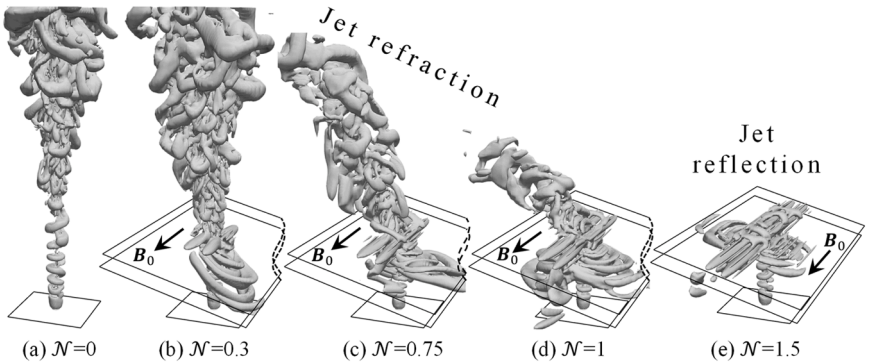

Fig. 4. Evolution of the submerged turbulent jet under an inclined (α=15°), localized DC magnetic field $\boldsymbol{B}_0$ with increasing interaction number: (a) $\mathcal{N}$=0; (b) $\mathcal{N}$=0.3; (c) $\mathcal{N}$=0.75; (d) $\mathcal{N}$=1; (e) $\mathcal{N}$=1.5.

process. Our analysis begins with experimental setups, such as the LIMMCAST facility using the low-melting-point Galinstan alloy, which enables detailed flow measurements under controlled magnetic field conditions [59]. Building on insights gained from these laboratory-scale models, we extend our investigation to industrial applications, specifically, thin slab continuous casting (TSC) with electromagnetic braking. This allows us to link fundamental flow behavior with practical flow control strategies employed in real casting operations.

Fig. 5 illustrates the setup of the LIMMCAST experiment. Fig. 5(a) shows the feeding of the Galinstan alloy into the mold cavity and the resulting flow pattern, including the position of the velocity probe at point P1 for the flow characteristics analysis. Fig. 5(b) details the EMBr position in the mold and the corresponding power distribution across its span. Fig. 5(c) highlights the electrical properties of the experimental setup, distinguishing between electrically conductive and insulating components. The solidified shell is modeled as a brass foil attached to the wide walls of the mold, replicating the semi-conductive boundary conditions relevant to the industrial slab casting process.

The liquid metal experiments replicated by numerical experiments showed that the interaction between the DC magnetic field and the turbulence strongly depends on the electrical properties of the domain boundaries. We have already shown in Fig. 3(a)-(b) that the isotropic turbulent eddies reorganize into coherent structures. In the presence of the domain boundaries (e.g. in the Plexiglass mold cavity in LIMMCAST), these structures reorganize into large-scale MHD vortices (see Fig. 6(a)) and propagate across the fluid domain. Such quasi-two-dimensional MHD structures exhibit self-sustaining behavior due to their interaction with induced electric current density lines [28].

The closure of induced electric current loops, either within the liquid bulk or through the semi-conductive solid shell in confined CC flows [28], is found to drive MHD effects that significantly modify the main flow pattern [27]. Consequently, the turbulent flow of conductive melt, along with the associated free-surface motion, can become unstable (Fig. 6(b)) or strongly dampened due to MHD forces. Additionally, under specific conditions, secondary flow structures may form near the meniscus, exhibiting transitional behavior [30].

From a numerical perspective, ensuring accurate conservation of the induced electric current density, especially at the interface between conductive and insulated media (Fig. 6(b)), is crucial. To address these challenges, the authors have systematically developed an MHD model capable of capturing key effects. The results of free-surface oscillations under MHD forces (Fig. 6(b)–(c)) demonstrate the robustness of the multiphase coupling algorithm [30]. The model effectively handles intense sloshing during wave collapse, accurately predicts the distribution of induced electric currents within the conductive fluid and properly terminates current lines at the wave surface boundary or within entrapped bubbles and droplets of the non-conductive phase (Fig. 6(c)). Fortunately, in real life, this behavior is observed only in non-conductive cavities, reaffirming the influence of the semi-conductive solid shell. Nevertheless, in the industrial CC process, MHD flows can remain unconstrained in regions such as the vicinity of electrically insulating SEN refractory walls.

Next, we present and discuss the LIMMCAST modeling results that are directly related to key phenomena observed in the CC process. Special attention is given to the role of the semi-conductive solid shell, which significantly influences the distribution of induced electric currents and the resulting MHD flow structures. These simulations bridge the gap between simplified laboratory-scale setups and the complex electromagnetic interactions occurring in industrial casting lines with EMBr practice.

Fig. 7 compares the influence of EMBr on turbulent flow and induced current behavior in the presence or absence of a semi-conductive solid shell. Fig. 7(a)-(b) show the surface velocity field without and with EMBr, respectively, highlighting the damping of turbulence and reduction in free surface fluctuations when the solid shell is considered. Fig. 7 (c)-(d) illustrate the distribution of induced electric current density lines. In the insulating-boundary case current loops stay in the bulk causing continuous “energy pumping” into MHD vortices and resulting in the strong fluctuations of the mold flow and meniscus, as discussed in the corresponding analysis of Fig. 6. The inclusion of a semi-conductive

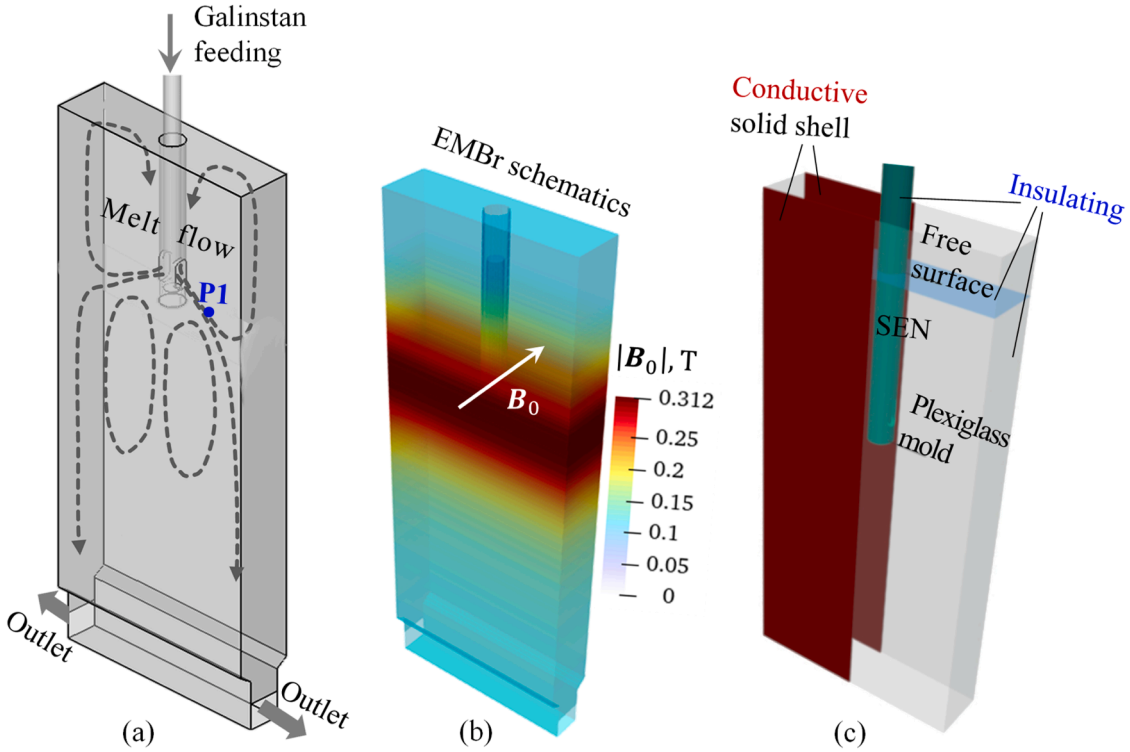

Fig. 5. Schematic of the LIMMCAST experiment: (a) Galinstan feeding and mold flow pattern with the location of probe point P1; (b) EMBr position and power distribution; (c) electrically conductive and insulating components of the setup, with the solidified shell attached to the wide faces.

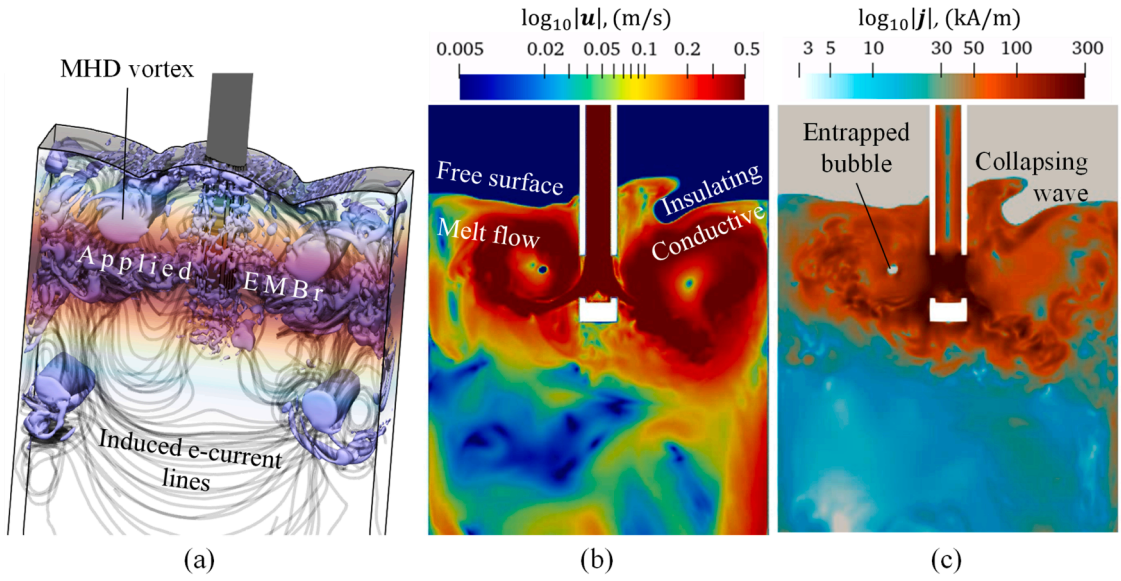

Fig. 6. Free-surface behavior in a non-conductive mold cavity under the applied EMBr: (a) self-inducing MHD vortices distorting the free surface in the CC mold interacting with the induced e-current lines; (b) velocity field and (c) induce e-current distribution at the meniscus region.

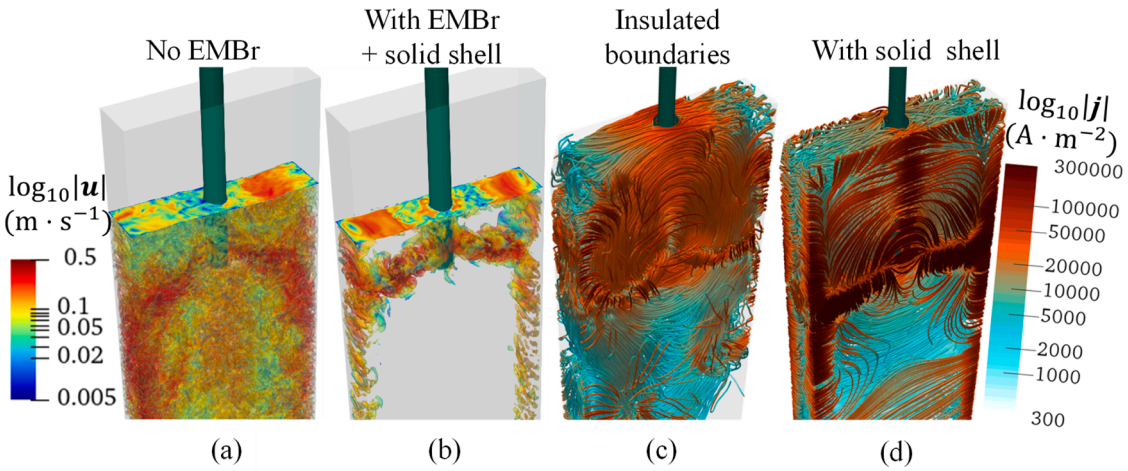

Fig. 7. Turbulent flow and free surface velocities: (a) without EMBr; (b) with EMBr considering the influence of the solid shell. Induced electric current density lines under an applied EMBr: (c) with electrically insulating boundaries; (d) accounting for the semi-conductive solid shell effects.

solid shell enables partial closure of current paths through the shell, leading to flow stabilization due to the Joule damping, corresponding to more realistic and industrially relevant representation of MHD behavior in continuous casting mold.

However, a comparative analysis of the results in Fig. 7(a)-(b) reveals that the actual meniscus velocities are not reduced when the EMBr of 312 mT is applied in the simulated LIMMCAST experiment test case. This cornerstone phenomenon will be addressed in a later section, as it is first essential to examine the fundamental restructuring of the turbulence spectrum inside the melt flow.

To quantify turbulence variations by comparing the melt flow without EMBr in Fig. 7(a) and under the applied EMBr of 312 mT in Fig. 7(b), the velocity field is recorded at monitor points, such as probe P1 in Fig. 5(a), within the liquid bulk during simulations. The turbulent spectrum results are shown in Fig. 8, combining the captured velocity magnitude time series (top subfigures) with a moving average (MA) using a window of $\Delta t = 0.2$sover an 8-second interval to highlight velocity oscillations. The power spectral density (PSD) illustrates the turbulent energy cascade (bottom subfigures), where low frequencies correspond to large, slow structures, and high frequencies represent small, fast ones. The red line indicates the dominant frequency f_1 on the PSD periodogram.

The fluid velocities inside the CC mold without a magnetic field in Fig. 8(a) exhibit strong oscillations with a long period. When EMBr is applied, the oscillation amplitude is dampened, and the flow fluctuates faster, as seen Fig. 8(c). The main flow oscillation frequency in the non-EMBr scenario in Fig. 8(b) is $f_1 = 0.77Hz$, corresponding to the low-frequency range where energy-containing vortex structures dominate. The blue dashed line in the PSD plots represents the classical $-5/3$ logarithmic decay in the inertial subrange of Kolmogorov's cascade, as experimentally observed by Saddoughi and Veeravalli [60]. With the application of a magnetic field, the dominant frequency f_1 increases up-to 5.63 Hz in Fig. 8(d) reflecting the damping of big slow vortices. Additionally, $a-3$ logarithmic decay (green dashed line), as reported by Kolesnikov and Tsinober [61], is observed in the higher-frequency inertial subrange. That serves as an indicator for 2D turbulence in MHD flow [62] presented earlier by results in Fig. 3(b).

The foundational studies by Kharicha et al. [26] on the evolution of free jets under a DC magnetic field were later extended to examine confined flows within the continuous casting mold [27]. As mentioned

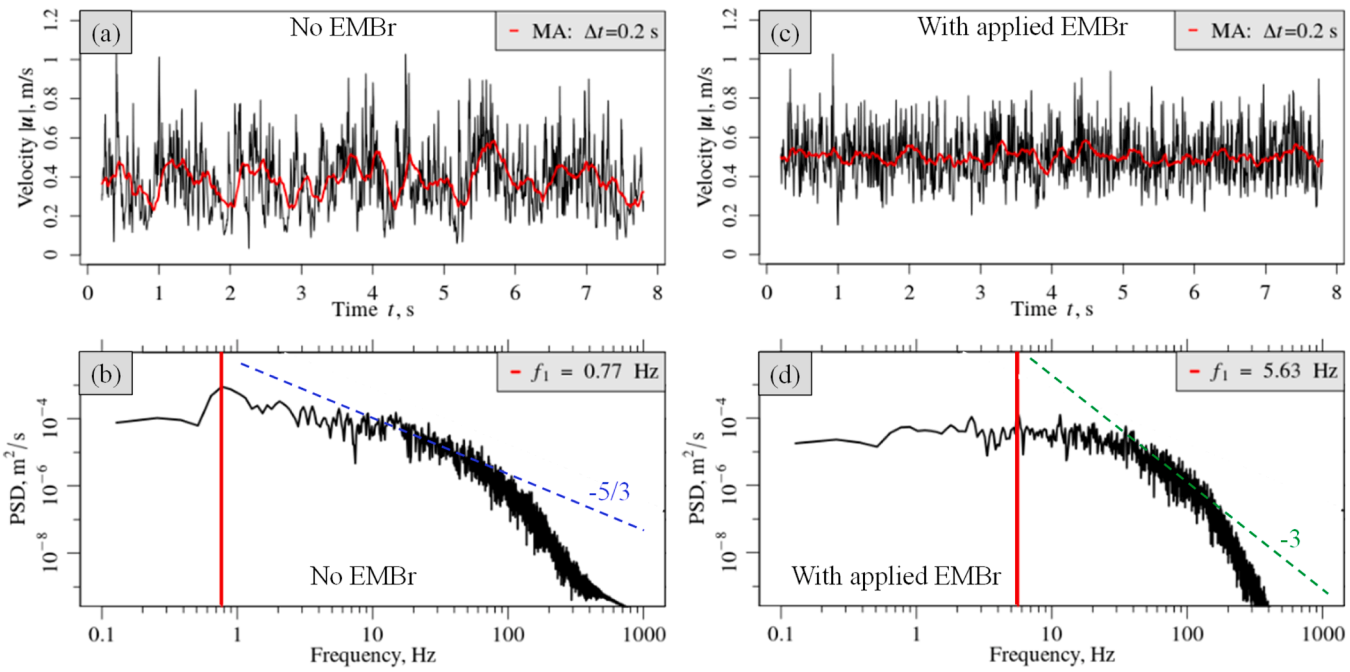

Fig. 8. Instantaneous velocity magnitude $|\boldsymbol{u}|$ (top subfigures) and power spectral density (PSD, bottom subfigures) at probe P1 in Fig. 5(a) for the cases: (a)-(b) without magnetic field; (c)-(d) with EMBr.

previously, these investigations were based on a series of GaInSn alloy experiments [52] conducted at the LIMMCAST facility at HZDR (Germany) [59,63,64], revealing a wide range of fluid motion patterns. As the liquid melt exits the SEN ports at an angle, its interaction with the EMBr field causes additional jet bending, as shown in Fig. 9(a). The feeding jet simultaneously bends and flattens with increasing magnetic field strength, forming a banana-shaped profile. This phenomenon was clearly observed in the LIMMCAST experiment using ultrasound Doppler velocimetry (UDV) by Schurmann et al. [65] and recently in more general study on MHD jets in crossflow in Jung et al. [66].

In the CC process, when the melt is introduced into the mold through the SEN, one or more highly turbulent jets are formed. This leads to the development of large recirculation zones above and below the SEN, commonly referred to as the double-roll pattern, as schematically shown for the LIMMCAST experimental setup in Fig. 5(a). The magnetic field, applied locally across the wide face of the mold cavity (see Fig. 5(b)), significantly influences flow behavior. The different regimes depicted in Fig. 9(b) were classified based on the Hartmann number ($\mathcal{H}a$), a dimensionless parameter commonly used to characterize MHD flows. The Hartmann number is defined as the ratio of electromagnetic to viscous forces:

$$\mathcal{H}a = |\boldsymbol{B}_0| \cdot L_0 \cdot \sqrt{\sigma/\mu}\,, \tag{22}$$

where, similarly to Eq. (21), L_0 is the characteristic length, σ is the electrical conductivity, and μ denotes the fluid's dynamic viscosity. The systematic studies revealed (see Fig. 9(b)) that as EMBr power increases: (i) initial reverse flow zones are formed above and below the SEN jets;

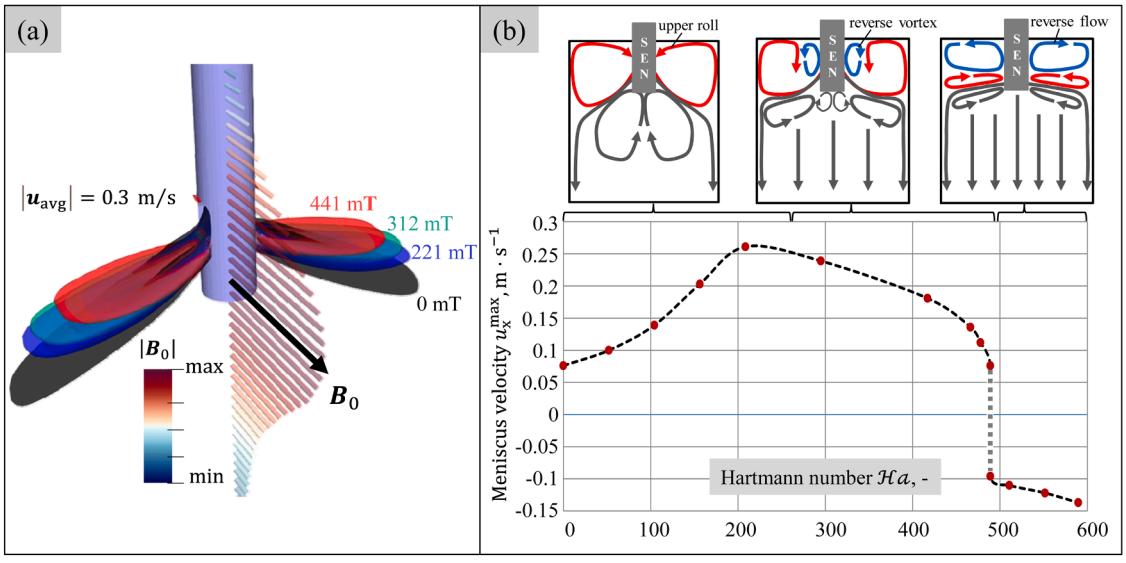

Fig. 9. Restructuring of the main flow patterns with the increasing EMBr power inside a CC mold: (a) consequent flattening and bending of the SEN feeding jets; (b) formation of the opposite vortices and the reverse meniscus flow (in blue). The transformation of the upper roll is marked in red.

(ii) these zones extend progressively towards the free surface; (iii) at higher Hartmann numbers $\mathscr{H}a$, the opposing flow along the top surface begins to dominate [27].

Additionally, in relation to the previously mentioned issue of meniscus acceleration under EMBr, the free surface plot in Fig. 9(b) indicates that the restructuring of turbulence into a more organized linear momentum within the upper roll initially leads to a "speedup." However, this is subsequently overtaken by the braking effect and momentum consumption caused by the formation of reverse flow structures. The observed phenomenon has been validated through both liquid metal alloy experimental studies and industrial observations. Numerical modeling offers a cost-effective alternative to practical trials, enabling precise optimization of EMBr parameters. Recently, Wang at al., [19] and Cui at al., [21,67] demonstrated this approach in thin slab casting simulations, examining how increasing EMBr power transforms a double-roll melt flow into a multi-roll pattern.

Fig. 10 presents the overall modeling setup used in the TSC simulations. Fig. 10(a) shows the geometric outline of the casting domain, including the mold and secondary cooling zones. Fig. 10(b) illustrates the distribution of the heat transfer coefficient (HTC) in the secondary cooling zone, which reflects the spatial variation in cooling intensity applied to the strand surface. The cooling conditions along the strand are defined by solving an inverse heat conduction problem (IHCP), developed by the co-authors [68], using a combination of OpenFOAM® and the BOBYQA optimization algorithm [69], based on laboratory measurements of water spray cooling. Fig. 10(c) plots the mold heat flux along the casting direction, corresponding to the thermal loading imposed by the water-cooled copper mold. Fig. 10(d) displays the solidification path implemented in the simulations, describing the evolution of solid fraction (f_s) as a function of temperature (T), which is essential for modeling the mushy zone behavior during shell formation. The material properties and additional casting parameters are listed in Table 1, where additional constants are the casting speed (U_{cast}),

Table 1
Material properties and casting conditions.

Property	Unit	Quantity
ρ	kgm^{-3}	7030
C_p	$Jkg^{-1}K^{-1}$	838.2
λ	$Wm^{-1}K^{-1}$	35
μ	Pas	0.0061
L	Jkg^{-1}	243,000
σ	Sm^{-1}	770,000
U_{cast}	$mmin^{-1}$	5.5
T_{cast}	°C	1551
T_{liq}	°C	1532
T_{sol}	°C	1496
Slab section	mm × mm	1200 × 100

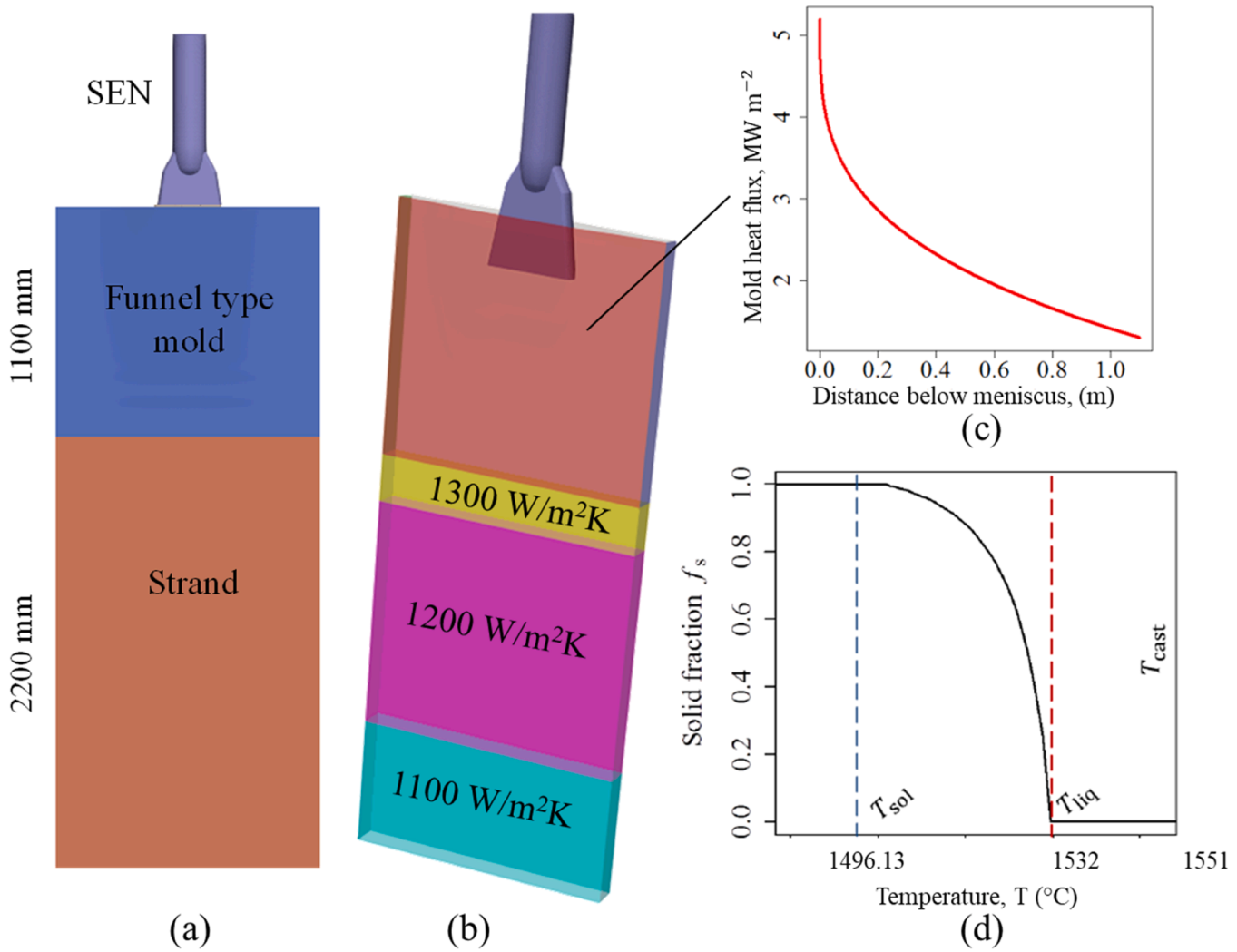

Fig. 10. Modeling setup for the TSC simulations: (a) geometry outline; (b) cooling conditions in the secondary cooling zone and (c) along the water-cooled copper mold; (d) solidification path used in the simulations, showing the relationship between solid fraction (f_s) and temperature (T).

pouring temperature (T_{cast}), liquidus (T_{liq}) and solidus (T_{sol}) temperatures.

The EMBr conditions will be presented later for each individual case, including the magnetic field distribution and the corresponding power input.

Fig. 11 illustrates the numerical mesh used for the TSC simulations. Fig. 11(a) presents a schematic view of mesh refinement across various regions of the domain, highlighting areas of increased resolution. Fig. 11 (b) provides a detailed view of the 3D mesh in the region surrounding the submerged entry nozzle with the overall mesh consisting of approximately 9 million volume elements. To accurately capture solidification phenomena and the closure of induced electric currents through the solid shell, the mesh boundary layers were applied along the mold and strand walls. Additionally, a mesh refinement strategy was implemented inside the SEN to resolve narrow gaps, enabling accurate modeling of turbulent flow structures and potential flow separation, as observed in supporting water model experiments. For the simulation setup, a single-port SEN design developed by RHI-Magnesita was used, commonly employed in modern thin slab and strip casting, where high throughput rates and rapid solidification are required. The external view of the SEN, with an immersion depth of 200 mm, is shown in Fig. 10(b), while the internal geometry details are provided in Fig. 11(b).

Extending from the lab-scale setups, presented earlier in this work, the electromagnetic brake is a widely used flow control technique in the real continuous casting process as a notable application of the DC magnetic field. A typical SEN/mold/EMBr setup for free-surface tracking simulations is shown in Fig. 12. The configuration features a local EMBr system with two poles positioned slightly apart (Fig. 12(a)). The time-averaged velocity field $|\boldsymbol{u}_{avg}|$ is presented in Fig. 12(b), comparing cases without a magnetic field (left subfigure) and with applied EMBr (right subfigure). The results show that MHD forces dampen the upper recirculation rolls, while the downstream flow becomes more uniform compared to the pronounced melt motion along the narrow walls in the absence of EMBr.

To provide a detailed comparison study, Fig. 13 summarizes key meniscus flow parameters, including the wave profile, superheat $\Delta T = T - T_{liq}$, temperature standard deviation STD(T), velocity magnitude $|\boldsymbol{u}|$, and velocity fluctuation STD($\boldsymbol{u}$). The standard deviation of the time series ζ_i for $i = 1, 2, \ldots, N$ is calculated as:

$$STD(\zeta_i) = \sqrt{\frac{1}{N}\sum_{i=1}^{N}(\zeta_i - \overline{\zeta})^2} \text{ with } \overline{\zeta} = \frac{1}{N}\sum_{i=1}^{N}\zeta_i, \tag{23}$$

where ζ_i is the value of the time-dependent variable at time t_i, N is the total number of time steps, and $\overline{\zeta}$ is the time-averaged mean.

These properties are analyzed along the interface isocontour (magenta line in Fig. 12(b)) for both cases. Firstly, Fig. 13(a) shows that the wave profile becomes shallower under EMBr, while the corner vortex intensifies due to MHD forces, leading to interface deformation. Secondly, the meniscus temperature increases under magnetic field action, as indicated by the superheat ΔT distribution in Fig. 13(b), compared to its counterpart in Fig. 13(c). Conversely, sub-meniscus velocity and its fluctuations are dampened with EMBr, along with temperature variations along the top surface. However, while velocity deviations decrease significantly, temperature fluctuations remain more persistent, suggesting flow pattern restructuring and the formation of new hot and cold zones, influencing superheat transport. Notably, the impact of EMBr on flow dynamics and superheat distribution varies depending on the SEN design, particularly at high throughput rates.

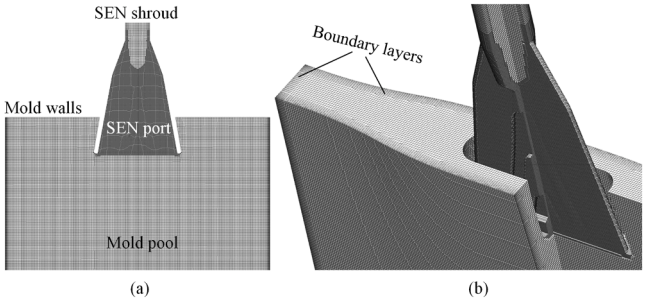

Fig. 11. Numerical grid used for TSC modeling: (a) schematic of mesh refinement across different regions; (b) detailed view of the 3D mesh in the SEN area with a total of 9 million volume elements.

Going even further, when combined with heat transfer and solidification models, numerical simulations become a powerful tool for analyzing the influence of MHD effects on undesired asymmetric flow patterns in thin slab casting (Fig. 14) and their impact on solid phase growth [70]. By capturing the intricate interactions between electromagnetic forces, fluid flow, and thermal gradients, these simulations provide valuable insights into superheat distribution, solidification front dynamics, and potential defects. This enables the optimization of EMBr configurations to enhance flow stability, improve heat transfer uniformity, and ultimately refine casting quality for industrial applications.

Fig. 14 presents the simulation setup used to investigate asymmetric flow conditions in continuous casting. Fig. 14(a) shows the configuration with a partially blocked SEN leading to uneven jet discharge and asymmetric mold flow. Fig. 14(b) depicts a misaligned SEN, another common industrial irregularity that distorts the jet trajectory and alters recirculation patterns. Fig. 14 (c) illustrates the distribution of the EMBr magnetic field applied in the simulations. This setup is used to evaluate the effectiveness of EMBr in mitigating the negative effects of asymmetric flow.

Fig. 15–16 presents the effects from both issues on thermal and solidification behavior in TSC, both with and without EMBr. Subfigures (a) and (b) show the temperature field distributions without and with EMBr, respectively. Subfigures (c) and (d) display the resulting shell thickness profiles. stabilizing influence of magnetic damping on the flow. Therse parameters are used to justify the effects from the EMBr application. Subfigure (e) shows the position and magnetic flux intensity of the applied EMBr field used in the simulation, responsible for the observed effects.

Extended studies revealed that EMBr application can either mitigate or exacerbate issues arising from asymmetric flow patterns in the CC mold [70]. While EMBr is generally employed to dampen turbulence and stabilize jet behavior, its influence is highly dependent on the underlying flow asymmetries. For instance, when a partial blockage of the SEN occurs, as illustrated in Fig. 15(a), the resulting deflected jet causes an uneven distribution of superheat across the mold. Once the magnetic field is applied, as shown in Fig. 15(b), the distorted flow pattern becomes effectively “frozen” due to the suppression of turbulent mixing. This can lead to a persistent thermal imbalance, which in turn promotes localized overheating and undesired one-sided remelting of the solidified shell, clearly visible in Fig. 15(d) [18].

Conversely, a non-uniform temperature distribution caused by the misalignment (tilting) of the SEN, as shown in Fig. 16(a), can often be effectively mitigated through the application of a symmetric EMBr, as demonstrated in Fig. 16(b). Such SEN misalignment may result from improper mounting, uneven wear, or thermal expansion of the tundish or supporting structures during prolonged casting operations. The tilted nozzle distorts the symmetry of the jet discharge, leading to preferential superheat transport to one side of the mold and resulting in uneven shell growth and increased risk of defects. When a symmetric EMBr is applied, the magnetic field acts to suppress the velocity fluctuations and turbulent instabilities associated with the asymmetric jet, promoting more uniform flow and thermal fields within the mold. In this case, the EMBr serves not only as a flow stabilizer but also as a corrective tool, restoring symmetry to the jet and recirculation rolls. The improved uniformity in the temperature field supports balanced shell formation and reduces thermal stress concentrations near the mold walls, which are often precursors to cracking or off-center bulging.

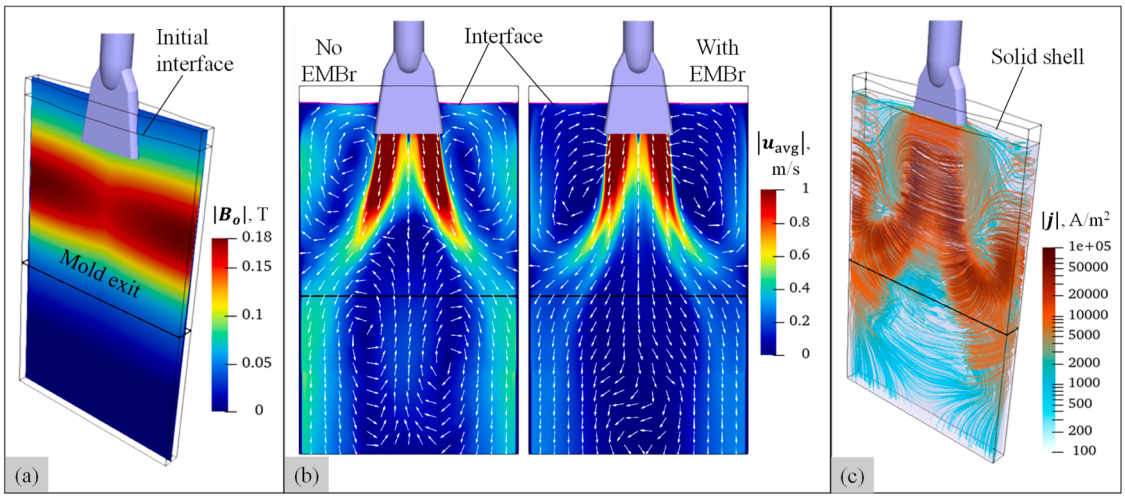

Fig. 12. Modelling results of free-surface behavior under EMBr in a thin slab continuous casting: (a) domain outline and EMBr schematics; (b) time-averaged velocity field $|\boldsymbol{u}_{\mathbf{avg}}|$ without (left) and with EMBr (right); (c) closure of induce electric current density lines through the solidified shell.

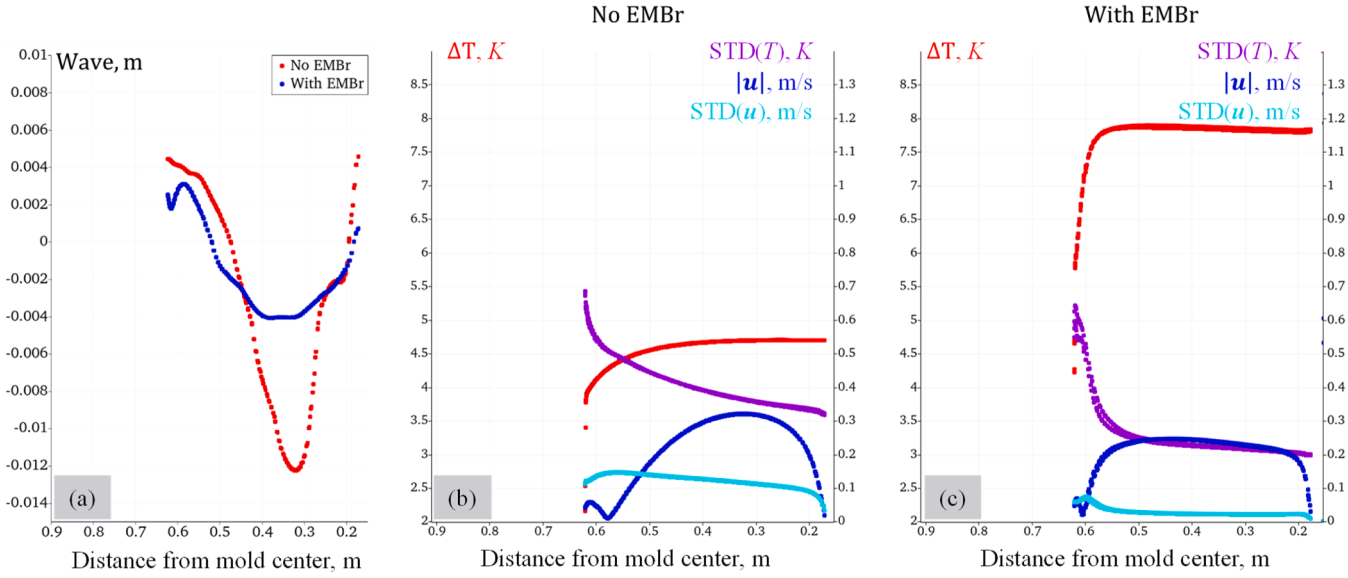

Fig. 13. Time-averaged distribution of key properties along the meniscus midline with and without EMBr: (a) wave profiles; (b)-(c) superheat ΔT, velocity magnitude $|\boldsymbol{u}|$, standard deviation of temperature STD(T), and velocity field fluctuations STD(u).

Such effects highlight the double-edged nature of magnetic damping in the presence of non-uniform inlet conditions. Therefore, to avoid reinforcing asymmetries and to maintain casting stability, adaptive or dynamically adjustable braking strategies must be employed [71]. These approaches allow real-time control over the magnetic field intensity and distribution, enabling compensation for transient or localized disturbances such as nozzle clogging, misalignment, or SEN wear. Integrating such intelligent control mechanisms into EMBr systems is becoming increasingly essential for high-quality, defect-minimized casting operations.

4. Conclusions

This study has provided a comprehensive analysis of the complex interactions between turbulent conductive melt flows and externally applied direct current (DC) magnetic fields within electromagnetic braking (EMBr) conditions in the continuous casting (CC) process. We have systematically examined how magnetohydrodynamic (MHD) forces reshape turbulence, transitioning from initially isotropic small-scale eddies to quasi-two-dimensional coherent structures. These mesoscopic transformations significantly influence macroscopic flow patterns, demonstrating a clear cascade from local turbulence modulation to global flow stabilization or destabilization, dependent on the induced electric current loops and the conductivity characteristics of the solidifying shell.

The interaction of turbulent jets with an applied DC magnetic field induces distinctive restructuring phenomena, notably flattening and bending of jet flows. Under strong magnetic fields, the turbulence is significantly suppressed in directions perpendicular to magnetic field lines, redistributing momentum and causing jets to broaden or flatten along these lines. Concurrently, if the applied magnetic field is inclined relative to the original jet axis, the jet undergoes bending or deflection due to the anisotropic distribution of Lorentz forces acting upon the flow. This bending is often accompanied by complex secondary flow structures, including reverse flow zones and vortices, arising from momentum conservation and current loop closures.

Our findings emphasize the importance of the induced current pathways, particularly highlighting the critical role of semi-conductive

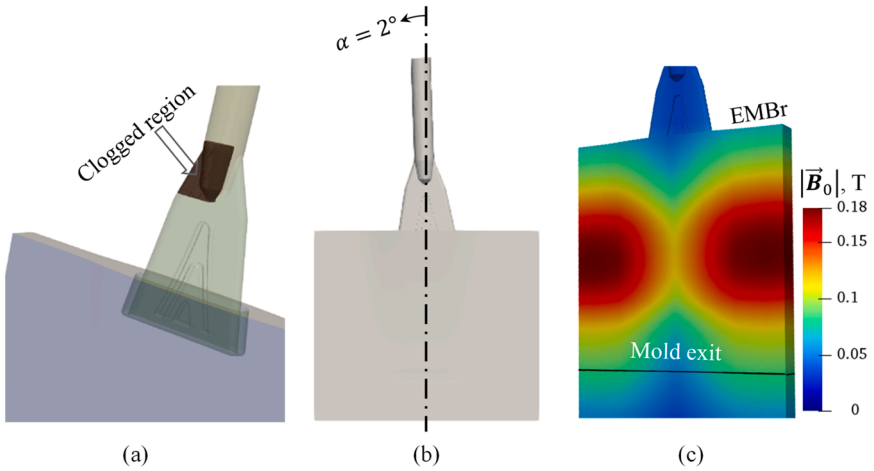

Fig. 14. Outline of the simulation setup used to model asymmetric flow caused by (a) a partially blocked SEN or (b) a misaligned SEN; (c) schematic of the EMBr magnetic field distribution.

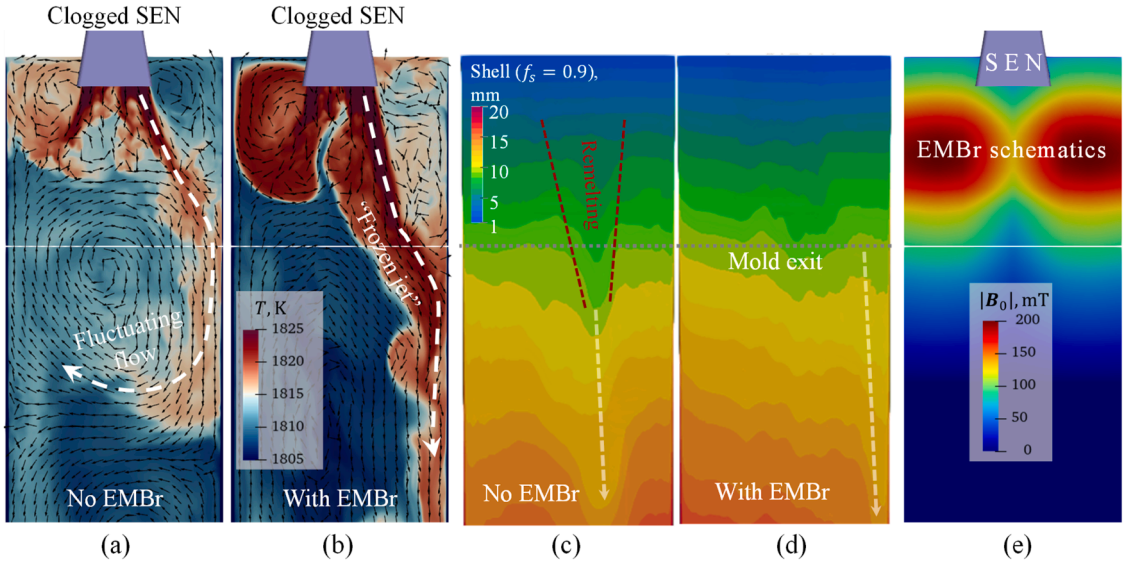

Fig. 15. Temperature field distribution in TSC under asymmetric flow caused by a partial blockage of an SEN: (a) without and (b) with the applied magnetic field. Corresponding shell thickness: (c) without and (d) with EMBr; (e) position and magnetic flux distribution of the applied EMBr field.

solid shells in guiding current closure and consequently altering flow dynamics. The results underscore the dual nature of MHD interactions, which can both dampen turbulent fluctuations and paradoxically exacerbate asymmetric flow phenomena under certain conditions. Notably, EMBr was shown to mitigate flow instabilities arising from submerged entry nozzle (SEN) misalignments but could conversely reinforce thermal asymmetries induced by partial nozzle blockages by "freezing" distorted flow patterns. Therefore, we emphasize the necessity of adaptive or dynamically adjustable EMBr strategies to manage transient irregularities and ensure consistent product quality.

The presented advanced numerical framework, integrating large eddy simulations (LES) with robust multiphase coupling, has proven essential for accurately predicting the complex interplay of turbulence, solidification, and electromagnetic phenomena. Such detailed modeling approaches are invaluable for capturing transient behaviors like jet oscillations, reverse flow formations, and meniscus instabilities, thus providing deeper insights into critical casting defect mechanisms.

Future work should focus on further refining turbulence modeling under strong magnetic field influences, particularly targeting improvements in predicting quasi-2D flow structures. Additionally, incorporating real-time adaptive EMBr control strategies and conducting extensive validation through cold metal experiments and full-scale industrial trials would enhance our understanding and practical management of MHD phenomena. By addressing these challenges, we can significantly improve the reliability and efficiency of EMBr applications, contributing to enhanced casting quality, defect reduction, and optimized metallurgical outcomes.

CRediT authorship contribution statement

Alexander Vakhrushev: Writing – original draft, Visualization, Validation, Software, Investigation, Formal analysis, Conceptualization. **Ebrahim Karimi-Sibaki:** Writing – review & editing. **Menghuai Wu:** Writing – review & editing, Project administration, Methodology, Formal analysis, Conceptualization. **Mohamad Al Nasser:** Writing – review & editing, Validation, Formal analysis. **Gernot Hackl:** Writing – review & editing, Supervision, Resources, Project administration, Funding acquisition, Data curation. **Yong Tang:** Writing – review & editing, Validation, Supervision, Methodology, Formal analysis, Data curation. **Josef Watzinger:** Writing – review & editing, Validation,

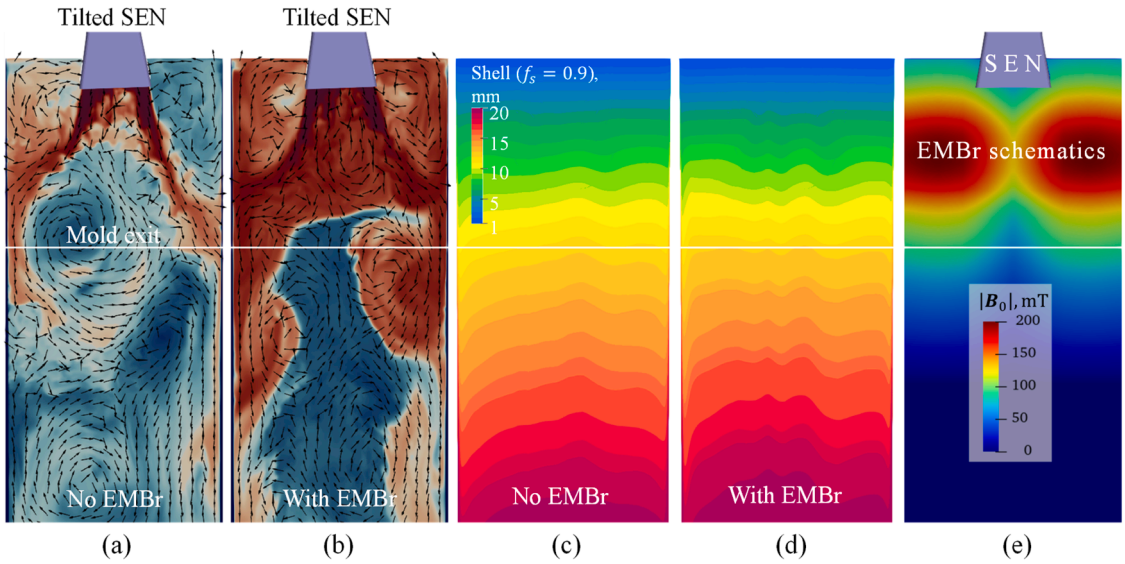

Fig. 16. Temperature field distribution in TSC under asymmetric flow caused by a misaligned SEN: (a) without and (b) with the applied magnetic field. Corresponding shell thickness: (c) without and (d) with EMBr; (e) position and magnetic flux distribution of the applied EMBr field.

Supervision, Resources, Project administration, Methodology, Funding acquisition, Data curation, Conceptualization. **Jan Boháček:** Writing – review & editing, Methodology, Investigation, Formal analysis, Conceptualization. **Abdellah Kharicha:** Writing – review & editing, Supervision, Resources, Project administration, Methodology.

Declaration of competing interest

The authors declare that they have no known competing financial interests or personal relationships that could have appeared to influence the work reported in this paper.

Acknowledgements

The authors acknowledge financial support from the Austrian Federal Ministry of Economy, Family, and Youth and the National Foundation for Research, Technology, and Development within the framework of the Christian Doppler Laboratory for Metallurgical Applications of Magnetohydrodynamics.

Data availability

No data was used for the research described in the article.

References

[1] P.D. Lee, P.E. Ramirez-Lopez, K.C. Mills, B. Santillana, Review: the "butterfly effect" in continuous casting, Ironmak. Steelmak. 39 (2012) 244–253, https://doi.org/10.1179/0301923312Z.00000000062.
[2] A. Vakhrushev, M. Wu, A. Ludwig, Y. Tang, G. Hackl, G. Nitzl, Numerical investigation of shell formation in thin slab casting of funnel-type mold, Metall. Mater. Trans. B. 45 (2014) 1024–1037, https://doi.org/10.1007/s11663-014-0030-2.
[3] K.C. Mills, P. Ramirez-Lopez, P.D. Lee, B. Santillana, B.G. Thomas, R. Morales, Looking into continuous casting mould, Ironmaking & Steelmaking 41 (2014) 242–249, https://doi.org/10.1179/0301923313Z.000000000255.
[4] B.G. Thomas, Review on modeling and simulation of continuous casting, Steel. Res. Int. 89 (2018) 1700312, https://doi.org/10.1002/srin.201700312.
[5] S.L. Mitchell, M. Vynnycky, Verified reduction of a model for a continuous casting process, Appl. Math. Model. 48 (2017) 476–490, https://doi.org/10.1016/j.apm.2017.04.004.
[6] M. Wu, A. Vakhrushev, A. Ludwig, A. Kharicha, Influence of forced convection on solidification and remelting in the developing mushy zone, IOP Conf. Ser.: Mater. Sci. Eng. 117 (2016) 012045, https://doi.org/10.1088/1757-899X/117/1/012045.
[7] B.G. Thomas, Modeling of continuous casting defects related to mold fluid flow, Iron Steel Technol. 3 (2006) 16.
[8] H. Yang, S.P. Vanka, B.G. Thomas, Mathematical modeling of multiphase flow in steel continuous casting, ISIJ Int 59 (2019) 956–972, https://doi.org/10.2355/isijinternational.ISIJINT-2018-743.
[9] S.-M. Cho, M. Liang, H. Olia, L. Das, B.G. Thomas, Multiphase flow-related defects in continuous casting of steel slabs, The Minerals, Metals & Materials Society. TMS 2020 149th Annual Meeting & Exhibition Supplemental Proceedings, Springer International Publishing, Cham, 2020, pp. 1161–1173, https://doi.org/10.1007/978-3-030-36296-6_108.
[10] P.E. Ramirez-Lopez, P.D. Lee, K.C. Mills, Explicit modelling of slag infiltration and shell formation during mould oscillation in continuous casting, ISIJ Int. 50 (2010) 425–434, https://doi.org/10.2355/isijinternational.50.425.
[11] P.E. Ramirez-Lopez, P.D. Lee, K.C. Mills, B. Santillana, A new approach for modelling slag infiltration and solidification in a continuous casting mould, ISIJ Int. 50 (2010) 1797–1804, https://doi.org/10.2355/isijinternational.50.1797.
[12] E. Torres-Alonso, R.D. Morales, L.G. Demedices, A. Nájera, J. Palafox-Ramos, P. Ramirez-Lopez, Flow dynamics in thin slab molds driven by sustainable oscillating jets from the feeding SEN, ISIJ Int 47 (2007) 679–688, https://doi.org/10.2355/isijinternational.47.679.
[13] E. Torres-Alonso, R.D. Morales, J. Palafox-Ramos, P. Ramírez-López, Oscillating jet flows in a thin slab mold and their influence on meniscus stability, Steel Res. Int. 79 (2008) 553–563, https://doi.org/10.1002/srin.200806166.
[14] W. Xiao, W. Chen, L. Zhang, Transient characteristics of slag entrainment and steel jet oscillation in a slab continuous casting strand with a straight bottom open submerged entry nozzle, Metall. Mater. Trans. B 56 (2025) 1744–1765, https://doi.org/10.1007/s11663-025-03442-w.
[15] R. Chaudhary, B.G. Thomas, S.P. Vanka, Effect of electromagnetic ruler braking (EMBr) on transient turbulent flow in continuous slab casting using large eddy simulations, Metall. Mater. Trans. B. 43 (2012) 532–553, https://doi.org/10.1007/s11663-012-9634-6.
[16] B.G. Thomas, S.M. Cho, Overview of electromagnetic forces to control flow during continuous casting of steel, IOP Conf. Ser.: Mater. Sci. Eng. 424 (2018) 012027, https://doi.org/10.1088/1757-899X/424/1/012027.
[17] S.M. Hosseini, E. Amani, An improved combination of ruler and local electromagnetic brakes for continuous casting process, J. Manuf. Process. 85 (2023) 1037–1053, https://doi.org/10.1016/j.jmapro.2022.12.030.
[18] A. Vakhrushev, A. Kharicha, E. Karimi-Sibaki, M. Wu, A. Ludwig, G. Nitzl, et al., Modeling asymmetric flow in the thin-slab casting mold under electromagnetic brake, Steel. Res. Int. 93 (2022) 2200088, https://doi.org/10.1002/srin.202200088.
[19] C. Wang, Z. Liu, B. Li, Effect of the intensity of single-ruler electromagnetic braking on the flow pattern in a thin-slab funnel mold, Metall. Mater. Trans. B 54 (2023) 3438–3450, https://doi.org/10.1007/s11663-023-02923-0.
[20] H. Lu, Y. Zhong, W. Ren, Z. Ren, Z. Lei, Effect of electromagnetic brake on transient asymmetric flow, solidification, and inclusion transport in a slab continuous casting, Steel Res. Int. 93 (2022) 2200518, https://doi.org/10.1002/srin.202200518.
[21] H. Cui, J. Sun, J. Zhang, H. Xu, G. Wang, Q. Liu, Large eddy simulation of various EMBr effects on the fluid flow, heat transfer and solidification process in an ultra-high speed thin slab casting mould with multi-port SEN, Ironmaking Steelmaking: Proc., Prod. Appl. (2024) 03019233241276912, https://doi.org/10.1177/03019233241276912.
[22] C. Wang, Z. Liu, G. Xu, B. Li, Z. Dou, Entrapment behavior of argon bubbles and non-metallic inclusions under combined magnetic fields in slab continuous casting, J. Mater. Res. Technol. 33 (2024) 9344–9356, https://doi.org/10.1016/j.jmrt.2024.11.258.

[23] B. Najafian Ashrafi, M. Barna, K. Timmel, T. Wondrak, C. Gruber, S. Eckert, Experimental study on the impact of traveling electromagnetic fields on the mold flow in a slab caster, Metall Mater Trans B (2025), https://doi.org/10.1007/s11663-025-03499-7.

[24] P.A. Davidson, Introduction to Magnetohydrodynamics, 2nd ed., Cambridge University Press, 2016, https://doi.org/10.1017/9781316672853.

[25] H. Kobayashi, Large eddy simulation of magnetohydrodynamic turbulent channel flows with local subgrid-scale model based on coherent structures, Phys. Fluids 18 (2006) 045107, https://doi.org/10.1063/1.2194967.

[26] A. Kharicha, A. Vakhrushev, E. Karimi-Sibaki, M. Wu, A. Ludwig, Reverse flows and flattening of a submerged jet under the action of a transverse magnetic field, Phys. Rev. Fluids 6 (2021) 123701, https://doi.org/10.1103/PhysRevFluids.6.123701.

[27] A. Vakhrushev, A. Kharicha, E. Karimi-Sibaki, M. Wu, A. Ludwig, G. Nitzl, et al., Generation of reverse meniscus flow by applying an electromagnetic brake, Metall. Mater. Trans. B. 52 (2021) 3193–3207, https://doi.org/10.1007/s11663-021-02247-x.

[28] A. Vakhrushev, A. Kharicha, Z. Liu, M. Wu, A. Ludwig, G. Nitzl, et al., Electric current distribution during electromagnetic braking in continuous casting, Metall. Mater. Trans. B. 51 (2020) 2811–2828, https://doi.org/10.1007/s11663-020-01952-3.

[29] S.-M. Cho, B.G. Thomas, Electromagnetic effects on solidification defect formation in continuous steel casting, JOM 72 (2020) 3610–3627, https://doi.org/10.1007/s11837-020-04329-8.

[30] A. Vakhrushev, E. Karimi-Sibaki, J. Bohacek, M. Wu, A. Ludwig, Y. Tang, et al., Impact of submerged entry nozzle (SEN) immersion depth on meniscus flow in continuous casting mold under electromagnetic brake (EMBr), Metals (Basel) 13 (2023) 444, https://doi.org/10.3390/met13030444.

[31] B.E. Launder, D.B. Spalding, The numerical computation of turbulent flows, Comput. Methods Appl. Mech. Eng. 3 (1974) 269–289, https://doi.org/10.1016/0045-7825(74)90029-2.

[32] T.-H. Shih, W.W. Liou, A. Shabbir, Z. Yang, J. Zhu, A new k-ϵ eddy viscosity model for high reynolds number turbulent flows, Comput. Fluids. 24 (1995) 227–238, https://doi.org/10.1016/0045-7930(94)00032-T.

[33] F.R. Menter, M. Kuntz, R. Langtry, Ten years of industrial experience with the SST turbulence model. Turbulence, Heat, and Mass Transfer 4, Begell House, Antalya, Turkey, 2003, pp. 625–632.

[34] J. Smagorinsky, General Circulation Experiments with the Primitive equations: I. The basic experiment, Mon, Wea. Rev. 91 (1963) 99–164, https://doi.org/10.1175/1520-0493(1963)091. <0099:GCEWTP>2.3.CO;2.

[35] J.W. Deardorff, A numerical study of three-dimensional turbulent channel flow at large reynolds numbers, J. Fluid. Mech. 41 (1970) 453–480, https://doi.org/10.1017/S0022112070000691.

[36] R. Chaudhary, C. Ji, B.G. Thomas, S.P. Vanka, Transient turbulent flow in a liquid-metal model of continuous casting, including comparison of six different methods, Metall. Materi. Trans. B 42 (2011) 987–1007, https://doi.org/10.1007/s11663-011-9526-1.

[37] C. Kratzsch, K. Timmel, S. Eckert, R. Schwarze, URANS simulation of continuous casting mold flow: assessment of revised turbulence models, Steel research int. 86 (2015) 400–410, https://doi.org/10.1002/srin.201400097.

[38] V. Yakhot, S.A. Orszag, S. Thangam, T.B. Gatski, C.G. Speziale, Development of turbulence models for shear flows by a double expansion technique, Phys. Fluids A: Fluid Dyn. 4 (1992) 1510–1520, https://doi.org/10.1063/1.858424.

[39] A. Vakhrushev, E. Karimi-Sibaki, M. Wu, A. Ludwig, G. Nitzl, Y. Tang, et al., Assessment of URANS-type turbulent flow modeling of a single port submerged entry nozzle (SEN) for thin slab continuous casting (TSC) process, Metall. Mater. Trans. B. 55 (2024) 891–904, https://doi.org/10.1007/s11663-024-03002-8.

[40] X. Miao, K. Timmel, D. Lucas, Z. Ren, S. Eckert, G. Gerbeth, Effect of an electromagnetic brake on the turbulent melt flow in a continuous-casting mold, Metall. Materi. Trans. B 43 (2012) 954–972, https://doi.org/10.1007/s11663-012-9672-0.

[41] O. Widlund, S. Zahrai, F.H. Bark, On MHD turbulence models for simulation of magnetic brakes in continuous steel casting processes, in: A. Alemany, Ph. Marty, J. P. Thibault (Eds.), Transfer Phenomena in Magnetohydrodynamic and Electroconducting Flows, Springer Netherlands, Dordrecht, 1999, pp. 61–76, https://doi.org/10.1007/978-94-011-4764-4_5.

[42] B.G. Thomas, R. Singh, S.P. Vanka, K. Timmel, S. Eckert, G. Gerbeth, Effect of single-ruler electromagnetic braking (EMBr) location on transient flow in continuous casting, J. Manuf. Sci. Prod. 15 (2015) 93–104, https://doi.org/10.1515/jmsp-2014-0047.

[43] C. Kratzsch, A. Asad, R. Schwarze, CFD of the MHD mold flow by means of hybrid LES/RANS turbulence modeling, J. Manuf. Sci. Prod. 15 (2015) 49–57, https://doi.org/10.1515/jmsp-2014-0046.

[44] F. Nicoud, F. Ducros, Subgrid-scale stress modelling based on the square of the velocity gradient tensor, Flow, Turbul. Combust. 62 (1999) 183–200, https://doi.org/10.1023/A:1009995426001.

[45] H.G. Weller, G. Tabor, H. Jasak, C. Fureby, A tensorial approach to computational continuum mechanics using object-oriented techniques, Comput. Phys. 12 (1998) 620–631, https://doi.org/10.1063/1.168744.

[46] C.M. Rhie, W.L. Chow, Numerical study of the turbulent flow past an airfoil with trailing edge separation, AIAA J. 21 (1983) 1525–1532, https://doi.org/10.2514/3.8284.

[47] J.H. Ferziger, M. Perić, Computational Methods For Fluid Dynamics, 3rd, rev. Ed ed, Springer, Berlin ; New York, 2002.

[48] M.-J. Ni, R. Munipalli, P. Huang, N.B. Morley, M.A. Abdou, A current density conservative scheme for incompressible MHD flows at a low magnetic reynolds number. Part II: on an arbitrary collocated mesh, J. Comput. Phys. 227 (2007) 205–228, https://doi.org/10.1016/j.jcp.2007.07.023.

[49] E.Mas de les Valls, Development of a simulation tool for MHD flows under nuclear fusion conditions, Tesi doctoral, Universitat Polit` ecnica de Catalunya, 2011. http://hdl.handle.net/2117/95157.

[50] C.W. Hirt, B.D. Nichols, Volume of fluid (VOF) method for the dynamics of free boundaries, J. Comput. Phys. 39 (1981) 201–225, https://doi.org/10.1016/0021-9991(81)90145-5.

[51] J.U. Brackbill, D.B. Kothe, C. Zemach, A continuum method for modeling surface tension, J. Comput. Phys. 100 (1992) 335–354, https://doi.org/10.1016/0021-9991(92)90240-Y.

[52] Y. Plevachuk, V. Sklyarchuk, S. Eckert, G. Gerbeth, R. Novakovic, Thermophysical properties of the liquid Ga–In–Sn eutectic alloy, J. Chem. Eng. Data 59 (2014) 757–763, https://doi.org/10.1021/je400882q.

[53] M. Rappaz, M. Bellet, M. Deville, Numerical Modeling in Materials Science and Engineering, Springer Berlin Heidelberg, Berlin, Heidelberg, 2003, https://doi.org/10.1007/978-3-642-11821-0.

[54] V. Favier, Modeling of Semisolid flow, in: comprehensive materials processing, Elsevier (2014) 191–209, https://doi.org/10.1016/B978-0-08-096532-1.00519-7.

[55] A. Vakhrushev, A. Kharicha, M. Wu, A. Ludwig, G. Nitzl, Y. Tang, et al., On modelling viscoplastic behavior of the solidifying shell in the funnel-type continuous casting mold, IOP Conf. Ser.: Mater. Sci. Eng. 529 (2019) 012081, https://doi.org/10.1088/1757-899X/529/1/012081.

[56] A. Vakhrushev, A. Kharicha, M. Wu, A. Ludwig, G. Nitzl, Y. Tang, et al., Modelling viscoplastic behavior of solidifying shell under applied electromagnetic breaking during continuous casting, IOP Conf. Ser.: Mater. Sci. Eng. 861 (2020) 012015, https://doi.org/10.1088/1757-899X/861/1/012015.

[57] P.A. Davidson, Magnetic damping of jets and vortices, J. Fluid. Mech. 299 (1995) 153–186, https://doi.org/10.1017/S0022112095003466.

[58] A. Vakhrushev, E. Karimi-Sibaki, M. Wu, A. Kharicha, Refraction and reflection patterns of an inclined turbulent conductive jet induced by a local transverse magnetic field, Appl. Math. Model. 145 (2025) 116124, https://doi.org/10.1016/j.apm.2025.116124.

[59] K. Timmel, C. Kratzsch, A. Asad, D. Schurmann, R. Schwarze, S. Eckert, Experimental and numerical modeling of fluid flow processes in continuous casting: results from the LIMMCAST-Project, IOP Conf. Ser.: Mater. Sci. Eng. 228 (2017) 012019, https://doi.org/10.1088/1757-899X/228/1/012019.

[60] S.G. Saddoughi, S.V. Veeravalli, Local isotropy in turbulent boundary layers at high reynolds number, J. Fluid. Mech. 268 (1994) 333–372, https://doi.org/10.1017/S0022112094001370.

[61] Yu.B. Kolesnikov, A.B. Tsinober, Experimental investigation of two-dimensional turbulence behind a grid, Fluid Dyn. 9 (1976) 621–624, https://doi.org/10.1007/BF01031323.

[62] J. Sommeria, R. Moreau, Why, how, and when, MHD turbulence becomes two-dimensional, J. Fluid. Mech. 118 (1982) 507, https://doi.org/10.1017/S0022112082001177.

[63] K. Timmel, S. Eckert, G. Gerbeth, Experimental investigation of the flow in a continuous-casting mold under the influence of a transverse, direct current magnetic field, Metall. Materi. Trans. B 42 (2011) 68–80, https://doi.org/10.1007/s11663-010-9458-1.

[64] K. Timmel, T. Wondrak, M. Röder, F. Stefani, S. Eckert, G. Gerbeth, Use of cold liquid metal models for investigations of the fluid flow in the continuous casting process, Steel. Res. Int. 85 (2014) 1283–1290, https://doi.org/10.1002/srin.201300034.

[65] D. Schurmann, I. Glavinić, B. Willers, K. Timmel, S. Eckert, Impact of the electromagnetic brake position on the flow structure in a slab continuous casting mold: an experimental parameter study, Metall. Mater. Trans. B 51 (2020) 61–78, https://doi.org/10.1007/s11663-019-01721-x.

[66] J. Jung, J. Moon, D. Kim, Dynamics of a Lorentz force activated oscillating jet, Phys. Rev. Fluids 10 (2025) 023701, https://doi.org/10.1103/PhysRevFluids.10.023701.

[67] H. Cui, J. Sun, J. Zhang, C. Ji, G. Wang, Q. Liu, Large eddy simulation of novel EMBr effect on flow pattern in thin slab casting mold with multi-port SEN and ultra-high casting speed, J. Manuf. Process. 133 (2025) 448–465, https://doi.org/10.1016/j.jmapro.2024.11.077.

[68] J. Bohacek, J. Kominek, A. Vakhrushev, E. Karimi-Sibaki, T. Lee, Sequential inverse heat conduction problem in OpenFOAM®, OpenFOAM J. 1 (2021) 27–46, https://doi.org/10.51560/ofj.v1.33.

[69] M.J.D. Powell, The BOBYQA algorithm for bound constrained optimization without derivatives. Department of Applied Mathematics and Theoretical Physics, Cambridge, England, 2009. http://www.damtp.cam.ac.uk/user/na/NA_papers/NA2009_06.pdf. accessed September 12, 2023.

[70] A. Vakhrushev, E. Karimi-Sibaki, M. Wu, Y. Tang, G. Hackl, J. Watzinger, et al., Effects of the asymmetric and oscillating turbulent melt flow on the heat transfer and solidification inside the thin slab continuous casting (TSC) mold under the applied electromagnetic brake (EMBr), J. Phys.: Conf. Ser. 2766 (2024) 012196, https://doi.org/10.1088/1742-6596/2766/1/012196.

[71] A. Vakhrushev, E. Karimi-Sibaki, M. Wu, A. Ludwig, G. Nitzl, Y. Tang, et al., Influence of the adjustable EMBr on the asymmetric flow in a thin slab caster with a misaligned SEN, IOP Conf. Ser.: Mater. Sci. Eng. 1281 (2023) 012026, https://doi.org/10.1088/1757-899X/1281/1/012026.